The Astrophysical Journal, 797:115 (33pp), 2014 December 20 doi:10.1088/0004-637X/797/2/115

HUBBLE SPACE TELESCOPE PROPER MOTION (HSTPROMO) CATALOGS OF GALACTIC GLOBULAR CLUSTERS. I. SAMPLE SELECTION, DATA REDUCTION, AND NGC 7078 RESULTS*

A. Bellini[1], J. Anderson[1], R. P. van der Marel[1], L. L. Watkins[1], I. R. King[2], P. Bianchini[3], J. Chanamé[4], R. Chandar[5], A. M. Cool[6], F. R. Ferraro[7], H. Ford[8], and D. Massari[7]

[1] Space Telescope Science Institute, 3700 San Martin Drive, Baltimore, MD 21218, USA; bellini@stsci.edu
[2] Department of Astronomy, University of Washington, Box 351580, Seattle, WA 98195, USA
[3] Max Planck Institute for Astronomy, Königstuhl 17, D-69117 Heidelberg, Germany
[4] Instituto de Astrofísica, Pontificia Universidad Católica de Chile, Av. Vicuña Mackenna 4860, Macul 782-0436, Santiago, Chile
[5] Department of Physics and Astronomy, The University of Toledo, 2801 West Bancroft Street, Toledo, OH 43606, USA
[6] Department of Physics and Astronomy, San Francisco State University, 1600 Holloway Avenue, San Francisco, CA 94132, USA
[7] Dipartimento di Fisica e Astronomia, Università di Bologna, via Ranzani 1, I-40127 Bologna, Italy
[8] Department of Physics and Astronomy, The Johns Hopkins University, 3400 North Charles Street, Baltimore, MD 21218, USA
Received 2014 August 27; accepted 2014 October 20; published 2014 December 5

ABSTRACT

We present the first study of high-precision internal proper motions (PMs) in a large sample of globular clusters, based on *Hubble Space Telescope* (*HST*) data obtained over the past decade with the ACS/WFC, ACS/HRC, and WFC3/UVIS instruments. We determine PMs for over 1.3 million stars in the central regions of 22 clusters, with a median number of ∼60,000 stars per cluster. These PMs have the potential to significantly advance our understanding of the internal kinematics of globular clusters by extending past line-of-sight (LOS) velocity measurements to two- or three-dimensional velocities, lower stellar masses, and larger sample sizes. We describe the reduction pipeline that we developed to derive homogeneous PMs from the very heterogeneous archival data. We demonstrate the quality of the measurements through extensive Monte Carlo simulations. We also discuss the PM errors introduced by various systematic effects and the techniques that we have developed to correct or remove them to the extent possible. We provide in electronic form the catalog for NGC 7078 (M 15), which consists of 77,837 stars in the central 2′.4. We validate the catalog by comparison with existing PM measurements and LOS velocities and use it to study the dependence of the velocity dispersion on radius, stellar magnitude (or mass) along the main sequence, and direction in the plane of the sky (radial or tangential). Subsequent papers in this series will explore a range of applications in globular-cluster science and will also present the PM catalogs for the other sample clusters.

Key words: globular clusters: individual (NGC 104 (47 Tuc, NGC 288, NGC 362, NGC 1851, NGC 2808, NGC 5139 (ω Cen, NGC 5904 (M 5, NGC 5927, NGC 6266 (M 62, NGC 6341 (M 92, NGC 6362, NGC 6388, NGC 6397, NGC 6441, NGC 6535, NGC 6624, NGC 6656 (M 22,), NGC 6681 (M 70), NGC 6715 (M 54), NGC 6752, NGC 7078 (M 15), NGC 7099 (M 30)) – proper motions – stars: kinematics and dynamics – stars: Population II – techniques: photometric

Online-only material: color figures, machine-readable tables

1. INTRODUCTION

Globular clusters (GCs) are the oldest surviving stellar systems in galaxies. As such, they provide valuable information on the earliest phases of galactic evolution and have been the target of numerous studies during the past century. Measures of the stellar motions in GCs, for instance, allow us to constrain the structure, formation, and dynamical evolution of these ancient stellar systems and, in turn, that of the Milky Way itself.

Almost all of what is known about the internal motions within GCs is based on spectroscopic line-of-sight (LOS) velocity measurements. Observations of the kinematics of GCs have come a long way since, e.g., Illingworth (1976) measured the velocity dispersions of 10 clusters using the broadening of absorption lines in integrated light spectra and Da Costa et al. (1977) measured the velocities for 11 stars in NGC 6397. The largest published samples today have velocities for a few thousand stars (e.g., Gebhardt et al. 2000; Malavolta et al. 2014; Massari et al. 2014).

Despite the major improvements provided by LOS-based studies on our understanding of the dynamics of GCs, there are some intrinsic limitations. First of all, the need for spectroscopy implies that only the brighter (more massive) stars in a GC can be observed. Moreover, in the crowded central regions of the cluster core, spectroscopy is limited by source confusion. Even integral-field spectroscopy is affected by the shot noise from the brightest sources. Moreover, LOS measurements are limited to measuring only one component of the motion, and therefore several model-dependent assumptions are required to infer the three-dimensional structure of GCs.

A significant improvement in data quality is possible with proper-motion (PM) measurements. Indeed, PMs have the potential to provide several advantages over LOS velocity studies: (1) no spectroscopy is required, so the more plentiful fainter stars can be studied, which yields better statistics on the kinematic quantities of interest; (2) stars are measured individually, in contrast with integrated light measurements, which contain a disproportionate contribution from bright giants; and (3) two components of velocity are measured instead of just one. More importantly, it directly reveals the velocity–dispersion anisotropy of the cluster, thus removing the mass-anisotropy degeneracy (Binney & Mamon 1982).

* Based on proprietary and archival observations with the NASA/ESA *Hubble Space Telescope*, obtained at the Space Telescope Science Institute, which is operated by AURA, Inc., under NASA contract NAS 5-26555.

PMs are small and difficult to measure with ground-based telescopes, where they require an enormous effort to achieve only a modest accuracy, particularly for faint stars in crowded fields (e.g., van Leeuwen et al. 2000; Bellini et al. 2009). On the other hand, the stable environment of space makes the *Hubble Space Telescope* (*HST*) an excellent astrometric tool. Its diffraction-limited resolution allows it to distinguish and measure positions and fluxes for stars all the way to the center of most GCs. Apart from small changes due to breathing, its point-spread function (PSF) and geometric distortion have been extremely stable over the two decades since the repair mission.

HST has the ability to measure PMs of unmatched quality compared with any ground-based facility, even in the most crowded central regions of GCs. Our team has developed methods to do this accurately (e.g., Anderson & King 2003a; Bellini et al. 2011). For instance, for a GC 5 kpc from the Sun, a dispersion of 10 km s^{-1} corresponds to ∼0.42 mas yr^{-1}; with a WFC3/UVIS scale of 40 mas pix^{-1}, this gives ∼0.1 pixel over a 10 year time baseline. Because our measurement techniques reach a precision of ∼0.01 pixel per single exposure for bright, unsaturated sources, a tenth of a pixel is easy game, even for rather faint stars, so large numbers of proper motions depend only on the availability of archival data. To date, detailed *HST* internal PM dynamics of GCs have been studied for only a handful of clusters: NGC 104 (47 Tuc, McLaughlin et al. 2006), NGC 7078 (M 15, McNamara et al. 2003), NGC 6266 (McNamara & McKeever 2011; McNamara et al. 2012), and NGC 5139 (ω Cen, Anderson & van der Marel 2010), but a deluge is now imminent; the project is described by Piotto et al. (2014), and the first result paper has been submitted (Milone et al. 2014).

With high-quality PM catalogs it will be possible to address many important topics for a large number of GCs such as: (1) *cluster-field separation*, for a better identification of bona fide cluster members for luminosity- and mass-function analyses and the study of binaries and exotic stars and to provide clean samples of targets for spectroscopic followup; (2) *internal motions*, to study in detail the kinematics and the dynamics of GCs in general and of each population component in particular (with the aim of looking for fossil signatures of distinct star-formation events); (3) *absolute motions*, by estimating an absolute proper-motion zero point using background galaxies as a reference frame (e.g., the series of papers starting with Dinescu et al. 1997 and continuing as Casetti-Dinescu and Bellini et al. 2010 using ground-based observations, and Bedin et al. 2003, Milone et al. 2006, and Massari et al. 2013 using the *HST*). Absolute PMs, in conjunction with radial velocities, allow calculation of Galactic orbits of GCs; at the same time the orbits that they exhibit are an indicator of the shape of the Galactic potential; (4) *geometric distance*, by comparing the LOS velocity dispersion with that on the plane of the sky (Rees 1995, 1997). This will provide a scale of GC distances that is independent of those based on stellar evolution or RR Lyrae stars; (5) *cluster rotation on the plane of the sky*, from the measure of the stellar velocities as a function of the position angle at different radial distances (e.g., Anderson & King 2003b);[9] (6) *energy equipartition*, from the analysis of stellar velocity dispersion as a function of the stellar mass (e.g., Trenti & van der Marel 2013); (7) *mass segregation*, by studying the stellar velocity dispersion as a function of the distance from the cluster center for different stellar masses; (8) *(an)isotropy*, by comparing tangential and radial components of the stellar motion; (9) *full three-dimensional cluster dynamics*, when LOS velocities are also known. The availability of all three components of the motion will directly constrain the three-dimensional velocity and phase-space distribution functions; and (10) *constraints on the presence of an intermediate-mass black hole*, by looking for both fast-moving individual stars and for a sudden increase in the velocity–dispersion profile near the center (e.g., van der Marel & Anderson 2010).

Unfortunately, the *HST* has executed only a very limited number of programs specifically aimed at the study of internal PM dynamics of GCs. Even so, many GCs have been observed with the *HST* for dozens of different studies, and several of these clusters have been observed on multiple occasions. Motivated by the enormous scientific potential offered by high-precision PM measurements of stars in GCs, we started a project to derive high-precision PM catalogs for all GCs with suitable multiepoch image material in the *HST* archive. This project is part of and uses techniques developed in the context of the *HST* proper-motion (HSTPROMO) collaboration[10], a set of *HST* projects aimed at improving our dynamical understanding of stars, clusters, and galaxies in the nearby universe through the measurement and interpretation of PMs (e.g., van der Marel et al. 2014).

The paper is organized as follows. In Section 2, we present the sample of GCs and data sets used for our study. In Sections 3, 4, and 5, we describe our detailed procedures for raw data reduction, astrometry, and PM measurements, respectively. In Section 6, we test the accuracy of our procedures on simulated data. Section 7 describes the effects of systematic errors and how we mitigate their effects. In Section 8, we discuss some of the kinematic quantities implied by the catalog of PMs for the GC NGC 7078 (M 15). Conclusions are presented in Section 9. Appendices present tables (available electronically) with listings of the *HST* data sets we used for each cluster and the NGC 7078 PM catalog.

This is the first of a series of several papers. Future papers in this series will present the PM catalogs for the other GCs in our sample, discuss the kinematic quantities they imply for these GCs, and address many of the scientific topics listed above.

2. SAMPLE SELECTION

This work is based on archival *HST* images taken with three different cameras: (1) the ultravioletvisible channel of the Wide-Field Camera 3 (WFC3/UVIS), (2) the wide-field channel of the Advanced Camera for Surveys (ACS/WFC), and (3) the high-resolution channel of ACS (ACS/HRC).

The physical characteristics of these cameras are as follows. The WFC3/UVIS camera is made up of two 4096 × 2048-pixel chips, with a pixel scale of about 40 mas pixel^{-1}. The ACS/WFC has the same number of resolution elements as the WFC3/UVIS, but it has a larger sampling of 50 mas pixel^{-1}. The ACS/HRC is the *HST* instrument with the finest resolution, being about 25 mas pixel^{-1}, and it is made up of a single chip of 1024 pixels on each side.

Wide-Field Planetary Camera 2 (WFPC2) exposures were not taken into account because despite the larger time baseline they can generally provide, there would only be a marginal increase in PM accuracy, due primarily to the larger pixel size (larger position uncertainties) and the smaller dynamical range of the

[9] Cluster rotations can also be measured spectroscopically; see, e.g., Peterson & Cudworth (1994); Bianchini et al. (2013).

[10] For details see the HSTPROMO home page at http://www.stsci.edu/∼marel/hstpromo.html.

Table 1
Globular Clusters and Their Parameters

Cluster ID	R.A.[a] (^{h}:^{m}:^{s})	Dec.[a] (°:′:″)	$D_\odot$[b] kpc	[Fe/H][b]	$E(B-V)$[b]	$\sigma_{V_{\rm LOS}}$[b] km s^{-1}	r_c[b] ′	r_h[b] ′
NGC 104 (47 Tuc)	00:24:05.71	−72:04:52.7	4.5	−0.72	0.04	11.0 ± 0.3	0.36	3.17
NGC 288	00:52:45.24	−26:34:57.4	8.9	−1.32	0.03	2.9 ± 0.3	1.35	2.23
NGC 362	01:03:14.26	−70:50:55.6	8.6	−1.26	0.05	6.4 ± 0.3	0.18	0.82
NGC 1851	05:14:06.76	−40:02:47.6	12.1	−1.18	0.02	10.4 ± 0.5	0.09	0.51
NGC 2808	09:12:03.10	−64:51:48.6	9.6	−1.14	0.22	13.4 ± 1.2	0.25	0.80
NGC 5139 (ω Cen)	13:26:47.24[c]	−47:28:46.45[c]	5.2	−1.53	0.12	16.8 ± 0.3	2.37	5.00
NGC 5904 (M 5)	15:18:33.22	+02:04:51.7	7.5	−1.29	0.03	5.5 ± 0.4	0.44	1.77
NGC 5927	15:28:00.69	−50:40:22.9	7.7	−0.49	0.45	8.8[d]	0.42	1.10
NGC 6266 (M 62)	17:01:12.78[e]	−30:06:46.0[e]	6.8	−1.18	0.47	14.3 ± 0.4	0.22	0.92
NGC 6341 (M 92)	17:17:07.39	+43:08:09.4	8.3	−2.31	0.02	6.0 ± 0.4	0.26	1.02
NGC 6362	17:31:54.99	−67:02:54.0	7.6	−0.99	0.09	2.8 ± 0.4	1.13	2.05
NGC 6388	17:36:17.23	−44:44:07.8	9.9	−0.55	0.37	18.9 ± 0.8	0.12	0.52
NGC 6397	17:40:42.09	−53:40:27.6	2.3	−2.02	0.18	4.5 ± 0.2	0.05	2.90
NGC 6441	17:50:13.06	−37:03:05.2	11.6	−0.46	0.47	18.0 ± 0.2	0.13	0.57
NGC 6535	18:03:50.51	−00:17:51.5	6.8	−1.79	0.34	2.4 ± 0.5	0.36	0.85
NGC 6624	18:23:40.51	−30:21:39.7	7.9	−0.44	0.28	5.4 ± 0.5	0.06	0.82
NGC 6656 (M 22)	18:36:23.94	−23:54:17.1	3.2	−1.70	0.34	7.8 ± 0.3	1.33	3.36
NGC 6681 (M 70)	18:43:12.76	−32:17:31.6	9.0	−1.62	0.07	5.2 ± 0.5	0.03	0.71
NGC 6715 (M 54)	18:55:03.33	−30:28:47.5	26.5	−1.49	0.15	10.5 ± 0.3	0.09	0.82
NGC 6752	19:10:52.11	−59:59:04.4	4.0	−1.54	0.04	4.9 ± 0.4	0.17	1.91
NGC 7078 (M 15)	21:29:58.33	+12:10:01.2	10.4	−2.37	0.10	13.5 ± 0.9	0.14	1.00
NGC 7099 (M 30)	21:40:22.12	−23:10:47.5	8.1	−2.27	0.03	5.5 ± 0.4	0.06	1.03

Notes.
[a] From Goldsbury et al. (2010), unless stated otherwise.
[b] From Harris 1996 (2010 edition), unless stated otherwise. $D_\odot$ is the GC distance from the Sun.
[c] From Anderson & van der Marel (2010).
[d] From Gnedin et al. (2002).
[e] From Beccari et al. (2006).

WFPC2 chips (fewer well-measured stars), particularly in the crowded cores, which is the focus of this study.

Ten GCs were specifically observed with the *HST* by some of us to study their internal motions, namely:

1. NGC 362, NGC 6624, NGC 6681, NGC 7078, NGC 7099 (GO-10401, PI: R. Chandar);
2. NGC 2808, NGC 6341, NGC 6752 (GO-10335 and GO-11801, PI: H. Ford);
3. NGC 6266, (GO-11609, PI: J. Chanamé); and
4. NGC 6715 (GO-12274, PI: R. P. van der Marel).

In 2011 January, we searched through the *HST* archive to look for other suitable data and additional GCs, imaged with the three mentioned cameras and with a total time baseline of at least two yr. Twelve GCs were found that satisfied these two criteria, and we successfully submitted an archival *HST* proposal (AR-12845, PI: A. Bellini) to analyze them. The clusters are NGC 104, NGC 288, NGC 1851, NGC 5139, NGC 5904, NGC 5927, NGC 6362, NGC 6388, NGC 6397, NGC 6441, NGC 6535, and NGC 6656. A summary of the general properties for all 22 GCs is given in Table 1. A complete list of observations used for our analysis of each cluster can be found in Appendices A and B.

3. DATA REDUCTION

3.1. Measuring Stellar Position and Fluxes in Each Exposure

This work is based solely on `_flt` or `_flc` type images. These images are produced by the standard *HST* calibration pipeline *CALWF3* (for WFC3) or *CALACS* (for ACS). Images of type `_flt` are dark- and bias-subtracted and flat-fielded, but not resampled (like the `_drz` type images); `_flc` images are `_flt` exposures that are also corrected for charge-transfer efficiency (CTE) (see below). The choice to use nonresampled images is motivated by the fact that we need to retain information about where exactly a photon hit the detector in order to minimize systematic errors in the PMs.

3.1.1. Charge-transfer Efficiency Corrections

Charge-transfer errors arise from the damaging effects of cosmic rays on the detectors. CTE losses affect both the shape (and therefore position) and the measured flux of stars, and these errors increase over time (see, e.g., Anderson & Bedin 2010). CTE effects are more severe when the image background is low, e.g., for short exposures or when bluer filters are used. It is a crucial step to properly model and correct these CTE losses if we want to measure high-quality PMs.

The CTE correction for ACS is especially important on exposures taken after the camera was repaired in 2009 (seven yr after its installation), whereas CTE damage is only mild or marginal on earlier exposures. For the WFC of ACS, the CTE correction is already included in the *CALACS* pipeline (`_flc` extension). The correction is not available for the HRC of ACS, but this is only a minor issue because the HRC stopped operating in 2006, and it was not repaired during the last *HST* Service Mission 4 (SM4). Moreover, the HRC readout also has a maximum of 1,024 transfers, so at its worst, its CTE losses are only half as bad as the WFC.

An official CTE correction for WFC3/UVIS has recently been made available, but it had not been implemented within the WFC3 calibration pipeline at the time of our reductions, so we manually corrected each individual WFC3/UVIS `_flt` exposure with the stand-alone CTE correction routine available on the official UVIS Web site[11] to create _flc images.

3.1.2. ACS/WFC

All ACS/WFC _flc images were reduced using the publicly available FORTRAN program img2xym_WFC.09x10, which is described in detail in Anderson & King (2006a).[12] The program does a single pass of finding and measures each star in each exposure by fitting a spatially varying effective PSF, ignoring any contribution from neighbors.

Library PSFs for several filters are provided along with the reduction software. To take into account the variation of the PSF across the field of view (FoV), the library PSFs are made up of an array of 9×10 PSFs across the detector. At any given location on the detector, the local PSF is then obtained through a bilinear interpolation of the four surrounding library PSFs.

During its ∼90 minute orbital period around the Earth, the *HST* is cyclically heated by the Earth and Sun. As a result, the focal length changes slightly during each orbit. This effect, known as "telescope breathing, affects the shape of the PSF in a nonconstant way across the FoV. To take into account the time-dependent variations of the PSFs, for each individual exposure we derived an additional array of up to 5×5 perturbation PSFs by modeling the residuals of library-PSF-subtracted stars across the detector. These perturbation PSFs were then interpolated into the 9×10 array of the library PSFs and added to them. The final set of PSFs (one set for each exposure) was then used to fit stellar profiles.

3.1.3. WFC3/UVIS

Star positions and fluxes on WFC3/UVIS images were measured with the software img2xym_wfc3uv, adapted mostly from img2xym_WFC.09x10. Library spatially varying PSFs are also available for this detector (in an array of 7×8 PSFs). As done for the ACS/WFC, we derived an additional array of perturbation PSFs for each WFC3/UVIS exposure and combined it with the library PSFs to fit stellar profiles. (For a more comprehensive analysis of spatial and time variations of UVIS PSFs, see Sabbi & Bellini 2013).

3.1.4. ACS/HRC

The measurement of stellar fluxes and positions in each ACS/HRC image was performed by using the publicly available routine img2xym_HRC and library PSFs. Because of the small FoV of HRC, there was no need to create spatially varying PSFs, and a constant PSF for each filter is adequate to properly represent stellar profiles all across the detector. We investigated the possibility of taking into account the time-dependent part of the PSFs but found that perturbation PSFs were able to provide only a negligible improvement in modeling stellar profiles.

3.2. Single-exposure Catalogs

The img2xym routine family used here produces a catalog of positions and fluxes of each measured star in each individual exposure, together with some other additional quantities and diagnostics, such as the quality-of-fit (QFIT) parameter, which tells us how well a source has been fit with the PSF model (Anderson et al. 2008).

Neighbor subtraction was not taken into account, so stars were measured as they are on the exposures. Our aim is to measure PMs as precisely as possible, so we decided to focus our attention on relatively isolated stars, for which positions can be reliably measured on individual exposures. The positions of blended stars, or stars for which the profile is impaired by brighter neighbors, would be affected by systematics in any case (see Section 7.5).

The precision with which we are able to measure positions for well-exposed stars on a single image is on the order of $\lesssim 0.01$ pixels (see Section 5.2). This level of precision can be achieved thanks to the high quality of the carefully modeled, fully empirical PSFs at our disposal.

3.3. Geometric-distortion Corrections

Stellar positions in each individual exposure were corrected for geometric distortion using the state-of-the-art solutions available for ACS/WFC (Anderson & King 2006a), ACS/HRC (Anderson & King 2006b), and WFC3/UVIS (Bellini & Bedin 2009; Bellini et al. 2011). These corrections are able to provide distortion-free stellar positions with residuals on the order of $\lesssim 0.01$ pixel (about the same precision offered by the PSF fitting). This level of precision in the distortion solution depends strongly on the adopted PSFs and cannot be achieved with simple centroid-type approaches, with optics-based PSFs, or even with empirical PSFs that do not adequately treat the spatial variations of the PSFs.

WFC3/UVIS is affected by a chromatic dependence of the geometric distortion, and the effect is larger for the bluer filters (see, e.g., Figure 6 of Bellini et al. 2011). The problem likely resides in the fused-silica CCD windows within the optical system, which refract blue and red photons differently and exhibit a sharp increase in the refractive index in the ultraviolet regime.

We showed in Bellini et al. (2011) that there are negligible color-dependent residuals in the UVIS distortion solutions for filters redward of F275W. A similar chromatic dependence of the distortion solution might also be present for the bluer filters of ACS/HRC. To minimize this subtle systematic effect, we decided to exclude any exposure taken through filters bluer than F336W for UVIS and F330W for HRC.

The bluest filter available for ACS/WFC peaks at 435 nm (F435W), and no chromatic dependence of the distortion solution has been reported for this camera. The ACS/WFC, however, experienced a slight change in the geometric-distortion solution after it was repaired during SM4. Post-SM4 positional residuals obtained with pre-SM4 geometric-distortion solutions can be on the order of 0.05 pixels and therefore need to be corrected. We carefully modeled the post-SM4 deviation of the distortion solution with a look-up table of residuals.[13] The accuracy of the post-SM4 geometric-distortion solutions for the ACS/WFC is comparable with the pre-SM4 solution and is on the order of $\lesssim 0.01$ pixels.

4. THE MASTER FRAME

The 22 GCs for which we want to measure PMs all have different apparent size and core density. Moreover, most of the archival data come from projects with scientific goals other than high-precision astrometry. As a result, the data sets at our disposal are extremely heterogeneous in terms of cameras or

[11] http://www.stsci.edu/hst/wfc3/tools/cte_tools.
[12] http://www.stsci.edu/∼jayander/ACSWFC_PSFs/.
[13] http://www.stsci.edu/∼jayander/ACSWFC_PSFs/POST-SM4/.

filters used, chosen exposure time, dither strategy, number of exposures, and time baseline.

Despite the severe lack of similarity among the data sets, it is important to be able to measure PMs for all 22 clusters in a homogeneous and standardized fashion. This eases subsequent analyses and comparisons of the dynamical properties of each cluster. To obtain a homogeneous set of PM catalogs, we had to address several issues.

The first issue concerns the definition of the reference system (master frame) on which to register the stellar positions. The master frame needs to be defined in a consistent way for each cluster and to have the same properties. Luckily, there is one data set in common between all but one GC (NGC 6266): GO-10775, PI: A. Sarajedini. This data set has been reduced with software tools similar to the ones we employed here (for more details, see Anderson et al. 2008). Its astrophotometric catalogs are publicly available,[14] and their high quality and reliability are supported by several dozens of papers. Moreover, the GO-10775 data were taken in 2006 and usually lie in between the time baseline of the data sets of each cluster, thus limiting bias effects in computing PMs.

The GO-10775 catalogs have stellar positions in equatorial units and in ACS/WFC pixels (rescaled to be exactly 50 mas pixel^{-1}). The pixel-based reference frame has north up and east to the left and places the center of each GC (as defined in Harris 1996) at location (3000, 3000). To better exploit the GO-10775 catalogs as our reference systems, we applied the following three changes.

1. We modified the pixel scale from 50 to 40 mas pixel^{-1}, which is the WFC3/UVIS pixel scale and represents a compromise between the ACS/HRC and ACS/WFC pixel scales).
2. We shifted the cluster center positions to location (5000, 5000), in order to accommodate all overlapping data sets with GO-10775 (which have different pointings and orientations) without having to deal with negative coordinates.
3. We removed from the GO-10775 catalogs those stars for which the position was not well measured, following the prescriptions given in Anderson et al. (2008). In addition, we removed stars belonging to any of the following cases: (1) saturated stars; (2) stars fainter than instrumental magnitude[15] −5.7 in either F606W or F814W; (3) stars with positional error larger than 5 mas in either coordinate; (4) stars with photometric error larger than 0.2 mag in either filter; and (5) stars with o_V or o_I, i.e., the ratio of neighbor versus star light in the aperture greater than one.

Although a GO-10775 catalog is available for ω Cen, we decided instead to base its reference system on the GO-9442 data set (PI: A. Cool). The reason for this is twofold: (1) the GO-9442 field of view is nine times larger than that of GO-10775, and there are other projects (such as GO-10252) that overlap with GO-9442 but not with GO-10775, thus allowing PM measurements at larger radial distances; and (2) the GO-9442 observation strategy was very similar to that of GO-10775 in terms of dithering scheme, number of exposures, and exposure time. Only the chosen filters are different, based on the different scientific goals. Moreover, the data of GO-9442 were reduced by one of us (J. Anderson) with a preliminary version of the same software used to create the GO-10775 database. To transform the GO-9442 catalog into our reference system, we applied the same changes that were applied to the GO-10775 catalogs.

In order to obtain a reference system for NGC 6266, we noted that the data of GO-10210 were taken following an observing strategy very similar to that of GO-9442 for ω Cen. Therefore, we reduced GO-10120 following the prescriptions given in Anderson et al. (2008) to produce a star catalog analogous to those of GO-10775, and we applied the same three changes as for the GO-10775 data sets.

5. PROPER MOTIONS

In the simple situation of repeated observations taken in only two epochs, one can simply measure the average position of stars within each epoch and then obtain PMs as the difference in position between the second and the first epoch, divided by the time baseline. In reality, our data sets generally contain a varying number of epochs, sometimes with one exposure only. Even when there are multiple exposures within a given epoch (which may span several weeks), stars are usually measured through different filters and with different exposure timesand hence different signal-to-noise ratios and it is not trivial to properly determine an average position for them within each epoch. Therefore, we decided to treat each individual exposure as a stand-alone epoch and to measure PMs by fitting a straight line to the data in the position versus epoch space (essentially the so-called *central overlap* method, first proposed by Eichhorn & Jefferys 1971).

Our general strategy for measuring PMs can be summarized in five main steps: (1) measure stellar positions in each individual exposure, (2) cross-identify the same stars in all of the exposures where they can be found, (3) define a reference network of stars with respect to which we can compute PMs, (4) transform stellar positions onto a common reference frame, and (5) fit straight lines to the data for reference-frame position versus epoch to obtain PMs.

Steps (3), (4), and (5) are nested into each other, and each of them requires some iteration in order to reject discrepant observations and improve the PM measurements. The basic scheme of the iterative process is summarized in the flow chart of Figure 1. We have already discussed step (1) in Section 3; the following subsections will provide a comprehensive explanation of the subsequent steps.

5.1. Linking Master-frame to Single-catalog Stellar Positions

First of all, each star in the master-frame list needs to be identified in each individual exposure where it can be found. The cross-identification is performed by means of general six-parameter linear transformations. These allow us to transform stellar positions as measured in the individual exposures onto the reference system and associate them with the closest star in the master-frame list.

We match up stars that have moved in random directions as time has passed. To limit the number of mismatches, we considered only stars for which master-frame matches are within

[14] http://www.astro.ufl.edu/~ata/public_hstgc/databases.html.

[15] The instrumental magnitude is defined as $-2.5 \times \log(\mathrm{flux})$, where the flux in counts is the volume under the PSF that best fits a stellar profile. We will use instrumental magnitudes extensively throughout this paper because they offer an immediate sense of the signal-to-noise ratio of measured sources. As a reference, a typical *HST* central PSF value is ∼0.2 (i.e., 20% of the source flux is in its central pixel): this means that saturated stars (central pixel $\geqslant$55,000 counts) will have magnitudes brighter than instrumental magnitude $-2.5 \times \log(55{,}000/0.2) = -13.6$. Moreover, stars with instrumental magnitude −10 will have a signal-to-noise ratio of 100.

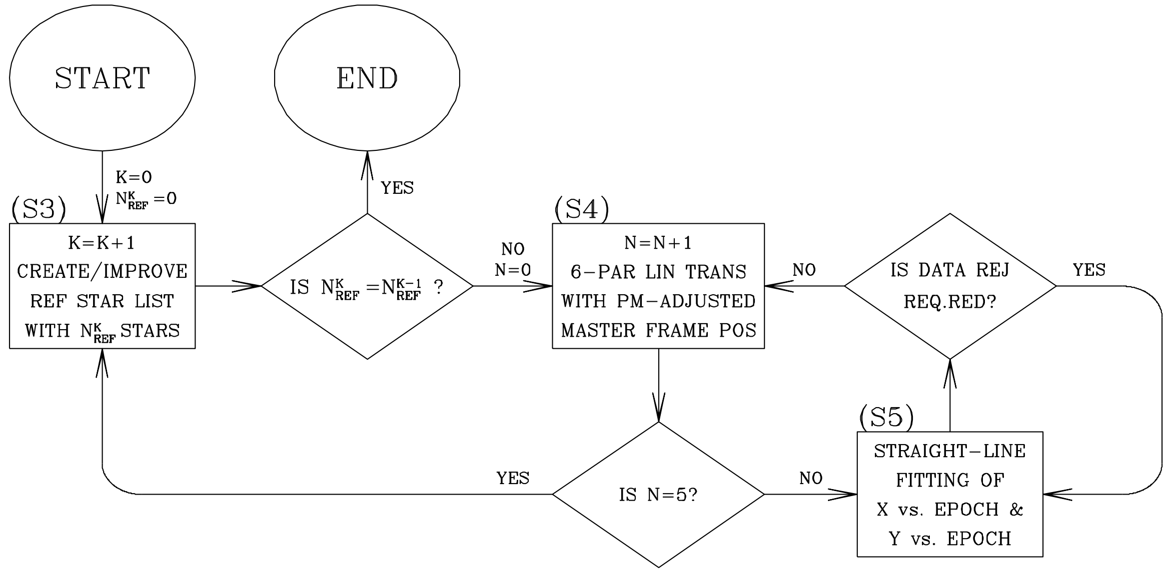

Figure 1. Flow chart illustrating the adopted scheme to compute PMs. The three main steps discussed in the text are marked as (S3), (S4), and (S5). See Sections 5.3, 5.4, and 5.5, respectively, for details.

2.5 pixels (0″.1). This criterion necessarily limits our ability to measure the motion of very fast-moving stars. As an example, let us take the NGC 5927 data set. The time baseline to the reference data set (GO-10775) is 3.87 yr for GO-9453 and about 4.38 yr for GO-11664 and GO-11729. The fastest motion we can measure for stars present only in the GO-10775 and GO-9453 data is $\mu = 2.5 \times 40/3.87$ mas yr^{-1} $= 25.84$ mas yr^{-1}. This limit is further reduced to 22.83 mas yr^{-1} if stars are measured in the GO-11664 or GO-11729 data sets but not in the GO-9453 one (see also Table 14). These PMs correspond to ∼940 km s^{-1} and 830 km s^{-1} at the distance of NGC 5927, but would correspond to smaller velocities for foreground stars.

At the initial stage, there is no need to fine tune the linear transformations, so long as we are able to identify master-frame stars in each exposure. We will later compute improved transformations to precisely place single-exposure stellar positions onto the master frame.

5.2. Expected Errors

Because each exposure corresponds to a stand-alone epoch, we cannot directly measure stellar positional errors from the rms of the residuals around an epoch-averaged position, as in the case of multiple exposures per epoch. Instead, we need to assign an a priori expected error based on some assumptions.

We reduced thousands of *HST* images and found, as expected, that there is a general trend of increasing positional rms as a function of the instrumental magnitude. This trend is stable over time and has little dependence on the filter used. For this reason, we decided to model this trend for the three *HST* detectors employed here and assign an expected positional error to each star of each individual catalog according to its instrumental magnitude.

To model the ACS/WFC expected-error trend, we chose the exposures of the core of ω Cen, a moderately crowded field containing several thousand stars and imaged through several dithered exposures in the F435W, F606W, and F814W filters (to sample the available wavelength coverage). For each filter, we computed average star magnitudes and positions and measured

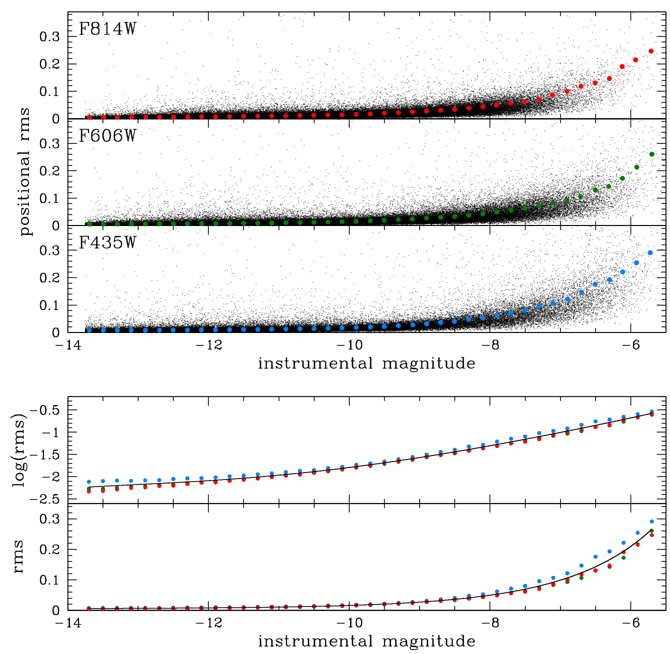

Figure 2. Modeling of the expected errors for the ACS/WFC camera. The top three panels show the one-dimensional positional rms as a function of the instrumental magnitude for three filters of the central field of ω Cen. We computed the 68.27 percentile of these rms in bins of 0.2 mag and fitted a fifth-order polynomial to them. The bottom two panels show the binned rms in linear and logarithmic units, together with the fitted function.

(A color version of this figure is available in the online journal.)

the positional rms of the residuals about the mean. Stars brighter than instrumental magnitude ∼−13.7 are saturated and were not taken into account. Stars fainter than ∼−5.7 are generally close to the shot-noise level for single-exposure measurements and define the faint limit of the model.

The top three panels of Figure 2 show the one-dimensional positional rms as a function of the instrumental magnitude for F814W, F606W, and F435W from top to bottom. We divided each sample of points into bins of 0.2 mag and computed a 3σ clipped 68.27 percentile of the positional rms within each bin (full colored circles). The bottom two panels of the figure show sampled values of the three filters, in linear and logarithmic units, as a function of the instrumental magnitude. The logarithmic units allow one to better distinguish the sampled values in the bright regime, whereas the linear units work better for the faint regime. A least-squares fifth-order polynomial is fit to the points in the log plane to model the positional rms trend. This model provides our expected errors for the ACS/WFC camera.

For the ACS/HRC and WFC3/UVIS cameras, we used the central fields of 47 Tuc and ω Cen, respectively,[16] and followed the same procedures used for the ACS/WFC camera to model the positional rms, and thus the expected errors, as a function of the instrumental magnitude. For these two detectors, we again modeled the expected errors using three filters: a blue, an intermediate, and a red filter. As for the ACS/WFC, the intermediate and red filters are the F606W and the F814W. As the blue filter for ACS/HRC, we chose F475W instead of the ACS/WFC F435W because F475W exposures are more numerous and have longer exposure times. Because the WFC3/UVIS detector covers bluer wavelengths than the ACS/WFC, the adopted blue filter was the F336W (which is also the bluest filter used to compute PMs). The average modeled curves of the expected errors for the ACS/HRC and the WFC3/UVIS cameras are very similar to those for the ACS/WFC shown in Figure 2.

5.3. The Reference-star List

At this stage in the reduction process, we are ready to start measuring PMs. We want to stress here that we will compute *relative* and not *absolute* PMs. The main reason is that the cores of GCs are so dense that the light of a background galaxy can hardly push itself above the scattered light of the cluster. (One of the few clusters in which there are enough galaxies to actually measure absolute PMs is NGC 6681; see Massari et al. 2013.) Therefore, in general we need to choose a reference set of objects other than background galaxies against which to measure motions. This leaves the cluster stars and the field stars. The cluster stars have a much tighter PM distribution, so they are the obvious choice. Our motions will thus be in a frame that moves and rotates with the cluster.

We want to use only the best-measured, unsaturated master-frame stars in order to minimize transformation residuals. Master-frame magnitudes are zero-pointed with respect to the deep exposures of GO-10775, so the short-exposure saturation limit in instrumental magnitudes is about −16.5, and the long-exposure limit is about −13.5. Stars between −16.5 and −13.5 mag are measured only in the short exposures. Generally, the best-measured stars lie within ∼3 mag of the saturation limit. Therefore, in principle, we could consider all stars between instrumental magnitude −16.5 and −10 in our reference list. However, because of the large variety of exposure times in our data sets, it could be that these bright stars are too bright (i.e., saturated) in some exposures. We therefore adopted a compromise by including fainter, less-constrained stars in the reference list to obtain an adequate number of reference stars for the transformations by extending the magnitude range of the reference-list stars to instrumental magnitude −8.

The process of creating the reference-star list is labeled as (S3) on the flow chart of Figure 1. We start by selecting cluster members on the basis of their positions on the color–magnitude diagram (CMD). To make the selection easier, especially for those clusters with high reddening foreground values, we corrected the master-frame photometry for differential reddening as done in Bellini et al. (2013), following prescriptions given in Milone et al. (2012). A few field stars will still be included, but once PMs are computed, we refined our reference-star list by removing from it those stars with PMs that are inconsistent with the cluster's bulk motion. This is an iterative process that ends when, from one iteration to the next, the number of stars in the reference list stops decreasing, meaning that we have computed PMs with respect to a list of bona fide cluster members that is as genuine as we can hope to obtain.

5.4. Positions on the Master Frame

For each exposure, we transformed the distortion-corrected positions of its stars into the master frame using general six-parameter linear transformations. Only bright, unsaturated reference stars in common between the single-exposure catalog and the master-frame catalog were used to compute the transformation parameters (i.e., reference stars that in the single-exposure catalogs are brighter than instrumental magnitude −9.5).

We chose to restrict the use of common reference stars to the same amplifier, to limit the impact of uncorrected geometric-distortion and CTE-mitigation residuals. The ACS/WFC and WFC3/UVIS cameras have four amplifiers each, corresponding to an area of 2048 × 2048 pixels. On the other hand, the ACS/HRC camera has only one amplifier, so this restriction does not apply.

The geometric distortion has a smooth variation across the detectors, and therefore it can be considered locally flat. If we were to use the local-transformation approach (see, e.g., Anderson et al. 2006; Bellini et al. 2009), we would have minimized the impact of uncorrected geometric-distortion residuals. However, the adopted amplifier-type restriction (a sort of semilocal approach) allows us to limit these effects. We will henceforth refer to the PMs thus obtained as "amplifier based". This is in contrast to "locally corrected" PMs, which are discussed in Section 7.3. Both types of PMs are listed in our catalogs. Which PMs are best depends on the specific scientific application.

Concerning CTE-correction residuals, y-CTE effects (i.e., trails along the Y axis of the detector) vary as a function of their distance from the register. Each amplifier has its own register. To date, there is no pixel-based x-CTE correction (i.e., trails along the X axis) available for *HST*. However, the impact of x-CTE effects is orders of magnitude smaller than that of y-CTE, and to the first order, it should be compensated for by our amplifier-based approach.

Because all of the stars in our reference list are moving in random directions with respect to each other with some dispersion, each and every transformed star position is affected by a systematic error of err $\propto \sqrt{\sigma_{\rm ref}/N_{\rm ref}}$, where $N_{\rm ref}$ is the total number of reference stars used for the transformation and $\sigma_{\rm ref}$ their PM dispersion. This implies that a large number of reference stars is best to minimize this source of error. On the other hand, it is not uncommon to have only a handful of reference stars to use for the transformations, especially in partially overlapping data sets or when the image depth is very different. A good compromise for the used data sets was found by rejecting all transformed stars that had less than 75 reference stars within their amplifier for ACS/WFC and WFC3/UVIS exposures and less than 50 for ACS/HRC exposures. In the vast

[16] No suitable ACS/HRC exposures of the core of ω Cen have been taken, whereas the core of 47 Tuc was used as the ACS/HRC calibration field.

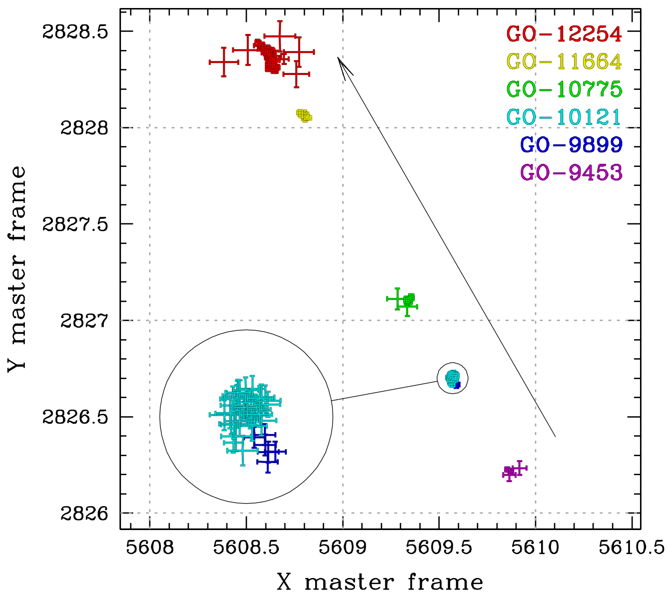

Figure 3. Transformed positions of a single star of the NGC 6752 data set, taken at six different epochs, as they appear on the reference system. Master-frame pixels are highlighted with dashed lines. Star positions and error bars are color-coded according to their program ID. Colors go from violet to green to red, moving from the 2002 to 2006 to 2011 epochs. A zoomed-in region of GO-9899 and GO-10121 positions is enclosed for clarity. An arrow shows the motion of the star during ∼nine yr.

(A color version of this figure is available in the online journal.)

majority of cases, the typical number of reference stars used for the transformations is larger than 300.

As mentioned, the reference stars themselves do also move. As a result, when we transform stellar positions of exposures taken years apart from the master-frame epoch, we will necessarily have to deal with larger transformation residuals. These residuals will in turn translate into larger uncertainties in the transformed positions of stars. We can bypass this problem by correcting the positions of the reference stars to correspond to the epoch of the single-exposure catalog that we want to transform.

Obviously, we need to know the PM of the reference stars to compute their position adjustments. As a consequence, computing positions on the master frame is an iterative process. With improved transformations we will be able to measure more precise PMs, and with them obtain even better transformations. We found that five iterations were enough to minimize the transformation residuals.

Once all of the stars of all of the exposures are transformed into the master frame, each master-frame star will be characterized by several slightly different positions, each of them referring to a different exposure (i.e., a different epoch). In Figure 3, we illustrate this concept for a rapidly moving star in the field of NGC 6752. On the master frame (the pixels of which are highlighted by dashed lines), each point represents a transformed single-exposure position. Error bars are obtained using expected errors (from Section 5.2) so that larger error bars refer to shorter exposure times. For clarity, we color-coded star positions according to their program number. The epochs of the observations go from 2002 (GO-9453, purple data) to 2011 (GO-12254, red data). We recall that the master-frame epoch is defined by the GO-10775 observations (in green). The actual master-frame position of this star lies underneath the green points (not shown). The data of GO-9899 and GO-10121 are separated by less than three months, and their position is magnified in the enclosed circle. An arrow indicates the motion of the star over ∼nine yr.

5.5. *Proper Motion Fitting and Data Rejection*

Let us suppose that for a given star we have N total positions in the master frame. Each position has an associated expected one-dimensional error and epoch of observation and is therefore characterized by the quadruplet (x_N, y_N, e_N, t_N). To measure the motion of this star along the X and Y axes, we used a weighted least-squares to fit a straight line to the data points (x_N, t_N) and (y_N, t_N). We progressively improved the fit by rejecting outliers or badly measured observations. This iterative straight-line fitting process is marked as (S5) in the flow chart of Figure 1.

We require that a star have at least four data points, with at least six months of time baseline between the second and the second-from-last point, in order for its PM to be measured. These conditions must be satisfied at every stage of the fitting and rejection process.

Before starting with the iterative process, we identify and reject obvious outliers. This task is done by removing one point at a time, then fitting the straight lines to the remaining $N - 1$ points. If the distance of a removed point from its associated fitted line is larger than 10 times its expected error, the point is rejected immediately. Such data points generally come from objects with a cosmic-ray event within their fitting radius. As a result, the centroid is shifted toward the cosmic ray, and their measured luminosity is enhanced by the cosmic-ray counts.

Let us suppose that a star still has N data points after these preliminary selections. We fit two weighted straight lines to the points (x_N, t_N) and (y_N, t_N). An example of these fits for the same star used in Figure 3 is illustrated in Figure 4. Data points are color-coded as in Figure 3. Panel (a) of Figure 4 shows the fitted line in the X position versus epoch plane, where the epoch of each point is expressed relative to the master-frame epoch (T = 0, in years). Panel (c) shows the fit for the Y position versus epoch. Panels (b) and (d) show the residuals (dx_N, dy_N) of the points around the straight-line fits.

To identify and reject the marginal outliers, we adopted the one-point-at-a-time approach as follows. We define error-normalized quantities $dx'_N = dx_N/e_N$, $dy'_N = dy_N/e_N$, and their sum in quadrature $r_N = \sqrt{{dx'_N}^2 + {dy'_N}^2}$. For a Gaussian distribution, the cumulative probability distribution of r_N is $P[r_N] = 1 - \exp(-r_N^2/2)$. Alternatively, if the enclosed probability is p_N, then $r_N = \sqrt{-2 \times \ln(1 - p_N)}$. For example, for $p = 0.6$ (the reference value we adopted), $r = 1.3537$. This means that in a two-dimensional Gaussian distribution, 60% of the points should be within 1.3537σ. Let the 60th percentile value of r_N of the data points be M. Then, to ensure that our residuals are consistent with the expected Gaussian, we would need to multiply all of our e_N values by a factor of $1.3537/M$. We let the rescaled, normalized residuals be (sx_N, sy_N).[17]

After the rescaling, to the lowest order the cloud of data points should be consistent with a two-dimensional Gaussian. Panel (e) of Figure 4 shows the distribution of the normalized and rescaled residuals (sx_N, sy_N). A circle of radius 1.3537 encloses 60% of the points (in gray). We now identify the outermost data point, at distance R. The probability that one data point has

[17] The rescaling can be done in principle using any percentile value. Our choice of using $p = 0.6$ is motivated by the fact that p needs to be small enough that the distribution is not sensitive to outliers, but p also needs to be large enough to guarantee good statistics.

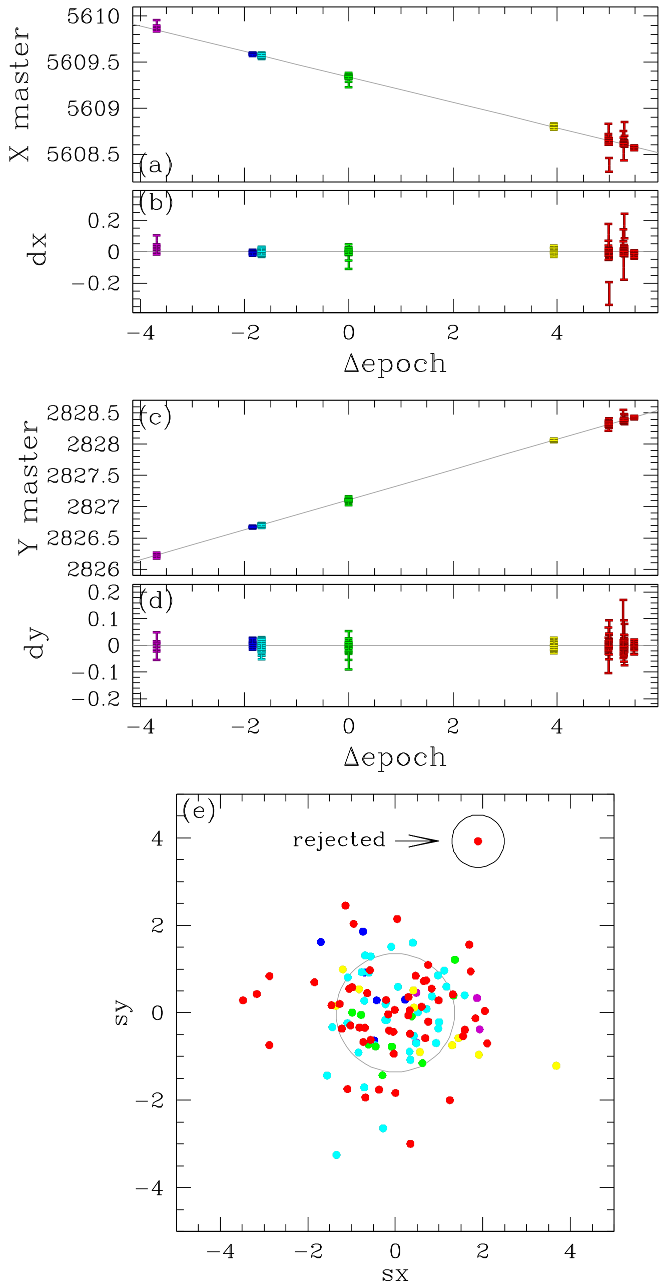

Figure 4. Illustrative example of the least-squares straight-line fitting procedure. The chosen star is the same as shown in Figure 3 (and points are color-coded accordingly). Panel (a) shows the X positions vs. the epoch of the observations with respect to the master-frame epoch, in Julian years. The fitted line is marked in gray. The residuals of the fit are in panel (b). Panels (c) and (d) show the same for the Y positions. Panel (e) illustrates the adopted rejection criterion. In the normalized and rescaled residual plane (sx, sy) (where points resemble a two-dimensional Gaussian), we identify the outermost point and check whether its probability of being that far out is inconsistent with that of a two-dimensional Gaussian distribution at a confidence level of 97.5%. If not, the data point is rejected (as in the example), and the straight-line fitting process is repeated without it.

(A color version of this figure is available in the online journal.)

such a high value of R is $P[1/1] = \exp(-R^2/2)$. Because there are N total points in the distribution, the probability of finding one data point out of N with such a high R is $P[1/N] = 1 - (1 - P[1/1])^N$. For example, if $R = 3$ then $P[1/1] \sim 1\%$, and $P[1/3] \sim N \times P[1/1]$. So, for $N = 10$ data points, there is a 10% chance of having a $\geqslant 3\sigma$ outlier.

We set a confidence threshold Q for accepting data points at 2.5%. If the data point with the highest R has $P[1/N] < Q$, then the data point is rejected and the straight-line fitting process is repeated. The iterations stop when all of the remaining data points are consistent with a two-dimensional Gaussian distribution. At this point, we also compute the errors of the slopes (proper motions) and intercepts of the fitted lines and the reduced χ^2 values. We report the PM errors measured in two distinct ways: (1) using the estimated errors as weights and (2) using the actual residuals of the data points around the fitted lines, as described in Section 6.1. It would also be possible to compute PM errors in a third, independent way, by multiplying the expected errors by the square root of the reduced χ^2 values, because all of these quantities are included in our PM catalogs.

To summarize, our rejection algorithm works as follows.

1. Preliminary rejection of obvious outliers;
2. Straight-line fitting to X and Y positions versus epoch;
3. Rescaling of normalized residuals to be consistent with a two-dimensional Gaussian distribution;
4. Checking whenever the outermost data point has $P[1/N] < Q$:
   (a) YES: reject the outermost data point, return to 2.
   (b) NO: continue.
5. Final straight-line fitting with the final set of acceptable data points to obtain the final straight-line-fit parameters and errors.

6. SIMULATIONS

In order to test the performance, accuracy, and reliability of our PM measurements, we carried out two types of simulations. The first simulation is based on a series of Monte Carlo tests that focus on our ability to reject outliers and obtain accurate values for the PMs and their errors. The second simulation tests our PM measurements in an artificial-star field representing a typical case, with GC stars and several field-star components, each of which has its own spatial density, bulk motion, and velocity dispersion.

6.1. Single-star Monte Carlo Simulations

Our Monte Carlo tests focus on the PM measurement of one single star, in cases where we have 10, 50, or 200 data points. For each case we run 100,000 random realizations in which data points span a time baseline of 5 yr. Two-thirds of the points are at t = 0, and the remaining are either randomly distributed or placed at the ends of the time baseline (±2.5 yr). Most of the data points have an assigned positional displacement that follows a Gaussian distribution with $\sigma = 0.01$ pixel. Five percent of the points are displaced with a dispersion 10 times larger, to mimic a population of outlier measurements, whereas an additional 5% of the points are misplaced by up to ±5 pixels, to mimic possible mismatches.

In each Monte Carlo run, individual observations were rejected based on the procedures described in Section 5.5, but the least-squares fits for the slope (the PM components μ_x and μ_y) and the intercepts (the positions at t = 0: $\overline{x}$ and $\overline{y}$) are computed with weights from the signal-to-noise-based error estimates from Section 5.2. The error estimates from each point are also used to compute errors in the motions and positions. For various reasons (cosmic rays, bad pixels, neighbors, and so on), individual observations can have errors that are larger than the

Table 2
Results of Monte Carlo Simulations[a]

Type	$\mathrm{err}_{\overline{x}}$	$\mathrm{err}_{\overline{y}}$	err_{μ_x}	err_{μ_y}
10 Data Points				
Monte Carlo rms	5.68	5.60	1.61	1.61
Average expected errors	5.09	5.13	1.46	1.47
Average residual-based	5.94	5.92	1.71	1.73
50 Data Points				
Monte Carlo rms	1.89	1.90	0.64	0.64
Average expected errors	1.87	1.86	0.63	0.63
Average residual-based	1.90	1.90	0.66	0.66
200 Data Points				
Monte Carlo rms	0.93	0.93	0.32	0.32
Average expected errors	0.92	0.92	0.32	0.32
Average residual-based	0.92	0.93	0.32	0.32

Notes.
[a] Units of 0.001 pixels for $\mathrm{err}_{\overline{x}}$ and $\mathrm{err}_{\overline{y}}$, and 0.001 pixel yr^{-1} for err_{μ_x} and err_{μ_y}.

expected errors, but not large enough to cause the observation to be rejected. To estimate the influence of these points on the errors in the measurements, we determine a residual for every point (using a fit to the four parameters that excludes that point) and adopt that residual as the estimate for the error in that determination. We then redetermine the errors in the slopes and intercepts using the same procedure as before. Because different observations have different effects on the slope and intercept determinations, this allows us to construct a more empirical estimate of the errors in the derived parameters.

Finally, for each of the three cases, we computed the Monte Carlo rms of the measured−true residual distribution for each of the derived quantities ($\mathrm{err}_{\overline{x}}$, $\mathrm{err}_{\overline{y}}$, err_{μ_x}, and err_{μ_y}) and compared them with the average of the two different error estimates. The results are shown in Table 2. In the case with 10 points, which resembles those data sets with few observations, the expected errors tend to underestimate the true errors, whereas the residual-based error estimates are more consistent with the true errors, although slightly larger. When more data points are available, both ways of computing the errors are in very good agreement with the Monte Carlo rms.

These results suggest that our fitting, rejection, and error-estimation algorithms are working well. Note that here we did not simulate the potential of small systematic errors (such as imperfect CTE corrections) in the bulk of the measurements. In reality, such errors will always be present at some level. The residual-based PM errors should therefore generally be more accurate than the PM errors based on assumed error estimates. The latter propagate only the random error in individual exposures and are unable to take into account small but present systematic errors.

6.2. Comprehensive Data Simulations

In order to test the automated procedure of converging on cluster-member-based PMs, the second simulation concerns the PM measurement and analysis of a field containing ∼19,000 simulated stars resembling cluster stars, field stars, and stars of two Milky Way satellite galaxies. Each star component has its own spatial density, proper motion, and velocity dispersion. We started by setting up the input master frame catalog, and then we extracted from it single-exposure catalogs simulating different exposure times, dithers, roll-angle orientations, cameras, and epochs.

6.2.1. The Input Master Frame

The spatial extension of the input master frame is 8000 × 8000 pixels and allows us to fully populate single-exposure catalogs with different dithers and roll-angle orientations. The CMD of cluster stars resembles that of a real cluster, but it was drawn by hand without aiming to be a reliable, physical representation of the real CMD of any actual GC. Panel (a) of Figure 5 shows the input CMD for cluster stars in instrumental magnitudes that for simplicity are called V and I. As for the real data sets, we run the simulation using instrumental-like magnitudes. All of the main evolutionary sequences are traced. We generated a total of 12,074 cluster stars, divided as follows: 9964 main-sequence (MS) stars (more numerous at increasing magnitudes), 350 subgiant branch (SGB) stars, 651 red giant branch (RGB) stars, 1,078 horizontal branch (HB) stars, and 31 white dwarf (WD) stars.

Cluster stars have a Gaussian-like distribution on the master frame (centered at position (5000, 5000)), to mimic the typical crowding conditions of the center of GCs. Moreover, their positional dispersion is larger at fainter magnitudes, to mimic some sort of mass segregation. The dispersion of MS stars grows from 344 to 600 pixels, while evolved stars have the same 344 pixel spatial dispersion as the bright MS stars.

The cluster's bulk motion is null by construction because all measured proper motions will be computed with respect to the bulk motion of the cluster. To resemble some sort of energy equipartition and test the quality of measured PM errors, we divided the MS into five groups and assigned to each of them an increasing velocity dispersion with fainter magnitudes. Velocity dispersions go from 0.01 pixel yr^{-1} for the brighter MS stars to 0.03 pixel yr^{-1} at the faint end. Evolved stars all have the same velocity dispersion as the bright MS stars. Panels (b1) to (b5) of Figure 5 show the vector point diagrams of cluster stars for the five different values of input velocity dispersion.

Because it is not uncommon to have Milky Way satellite stars superimposed on GC fields (e.g., Small Magellanic Cloud stars in NGC 104 and NGC 362, or Sagittarius dwarf spheroidal stars in NGC 6681 and NGC 6715), we included the presence of two such nearby galaxies. Panel (c) of Figure 5 shows their CMD. Galaxy stars are placed randomly with a flat distribution on the master frame. The brighter galaxy (GAL1) has 1126 stars and a bulk motion of (−0.12, −0.17) pixel yr^{-1}. We set its internal velocity dispersion to be small but still measurable: 5 milli-pixel yr^{-1}(i.e., 0.2 mas yr^{-1}). The faint galaxy (GAL2) has 685 stars and a bulk motion of (−0.25, 0.2) pixel yr^{-1}. We assigned no internal velocity dispersion to its stars: in this way we are able to obtain an external estimate of our measurement errors. Panel (e1) of Figure 5 shows the vector-point diagram of GAL1 stars; the black cross marks the location of the cluster's bulk motion. An arrow in panel (e2) points to the bulk motion of GAL2.

We generated three sets of field stars, named FS1 (1516 stars), FS2 (1273 stars), and FS3 (2057 stars). Each set has its own ridge line on the CMD (see panel (d) of Figure 5). Although cluster and galaxy stars do not have a color spread by construction (mimicking single-stellar populations), we introduced a Gaussian scatter ($\sigma \sim 0.5$ mag) to the color of field stars to resemble the fact that they are not at the same distance or do not have the same chemical composition.

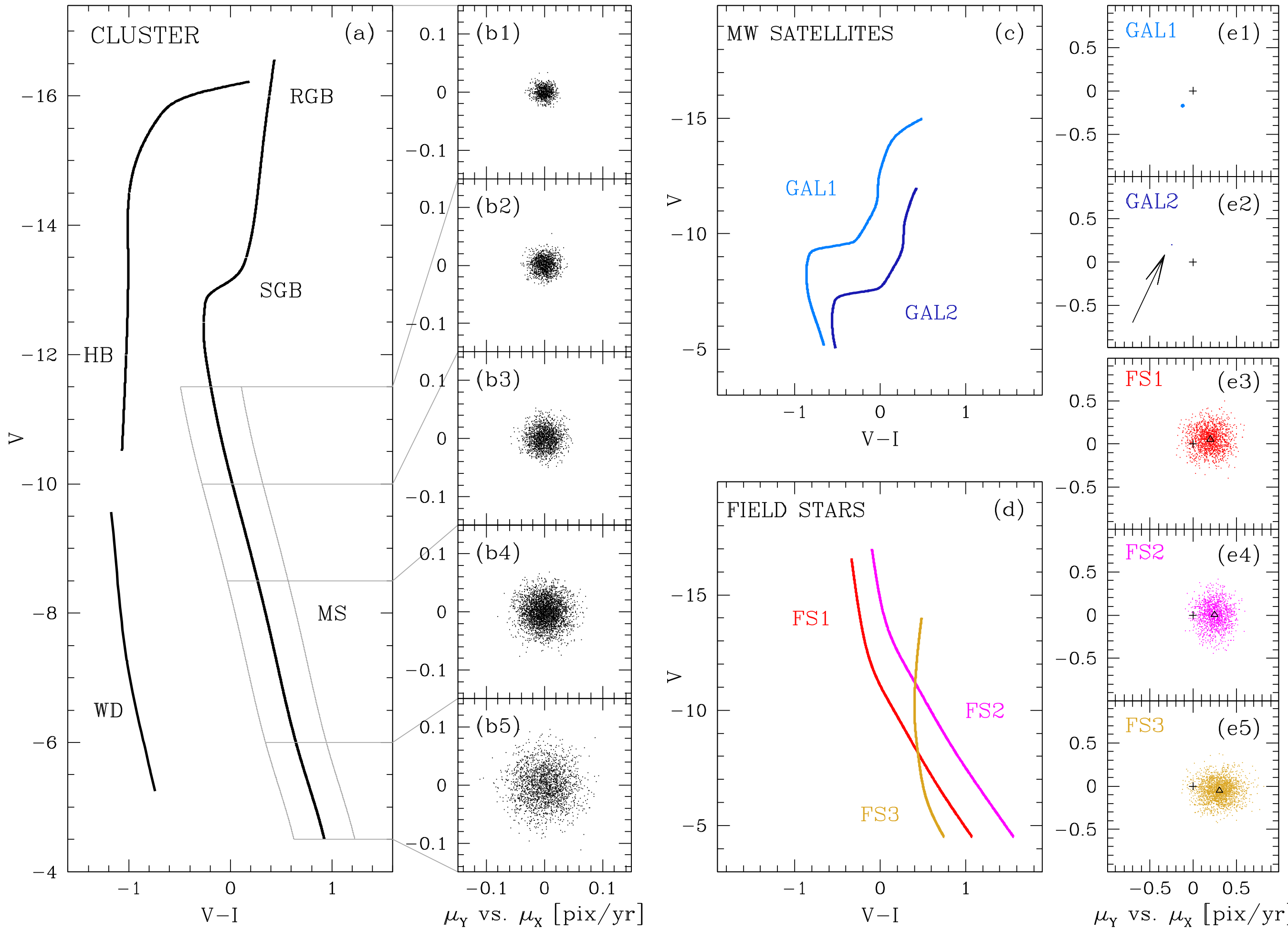

Figure 5. Color–magnitude and vector–point diagrams of the stars used for our comprehensive simulation. The CMD of cluster stars is in panel (a). All of the main evolutionary sequences have been included. We assigned to MS stars an increasing internal velocity dispersion at increasing magnitudes, to mimic some sort of energy equipartition. Panels (b2) to (b5) show the vector point diagrams of MS stars for four different values of the velocity dispersion. Bright MS stars and more evolved stars all have the same (smaller) velocity dispersion, as shown in panel (b1). We also simulated two Milky Way dwarf galaxies (GAL1 and GAL2, in azure and blue) and three components of field stars (FS1, FS2, and FS3 in red, magenta, and yellow, respectively). Their CMDs are in panel (c) and (d), respectively. We assigned a very small velocity dispersion (0.005 pixel yr^{-1}, 0.2 mas yr^{-1}) to GAL1 stars (panel (e1)) and no velocity dispersion at all to GAL2 stars (panel (e2)). Field stars have the largest velocity dispersion. We assigned a bulk motion (black triangle) to field stars in such a way that they partially overlap cluster stars in the vector point diagram (panels (e3), (e4), and (e5)).

(A color version of this figure is available in the online journal.)

The field FS1 has a bulk motion of (0.2, 0.05) pixel yr^{-1}, with a round velocity dispersion of 0.13 pixel yr^{-1}. The bulk motion of field FS2 is (0.25, 0.0) pixel yr^{-1}, with a X-velocity dispersion of 0.12 pixel yr^{-1} and a Y-velocity dispersion of 0.14 pixel yr^{-1}. For the field FS3, these three quantities are, respectively, (0.3, −0.05) pixel yr^{-1}, 0.14 pixel yr^{-1} and 0.12 pixel yr^{-1}. The vector point diagrams of field stars are shown in panels (e3), (e4), and (e5) of Figure 5). The bulk motion of each field component is marked by a triangle.

For clarity, Figure 6 shows the complete simulated vector-point diagram. Each component is color-coded as in Figure 5. The location of the bulk motion of GAL2 stars is highlighted by an open circle.

6.2.2. Single-exposure Catalogs

Now that the input master frame has been defined, we can extract single-exposure catalogs from it as follows. We set up five data sets spanning a total time baseline of 3.18 yr. Each epoch has its own orientation angle, offset (i.e., the center of the cluster is not always at the center of the pointing), dither pattern, magnitude zero point, and pixel scale (to simulate the three cameras (ACS/WFC, ACS/HRC, and WFC3/UVIS). In addition, we added small random variations to all of these quantities: up to 0.2% variation for orientation angle, scale (to mimic focus changes), and observing time (to mimic exposures taken within a few days), and up to ±40 pixels in either direction to resemble a dither pattern.

Table 3 lists the parameters adopted for each data set. The first two data sets mimic ACS/WFC exposures (and the second one is designed to be similar to GO-10775), the third refers to ACS/HRC exposures, and the WFC3/UVIS exposures are in data sets 4 and 5. The magnitude zero point Δmag listed in Table 3 is the difference in instrumental magnitude between input master stars and deep-exposure stars. Stars in the short exposures are 2.2 mag fainter than those in the deep ones. Offsets are in units of pixels in the raw-coordinate system of each catalog. We generated a total of 50 single-exposure catalogs.

Stars of each single-exposure catalog are selected from the input master frame according to their positional parameters (roll angle, scale, offsets), and a magnitude zero point is applied. The positions of the stars are then decorrected for geometric distortion and put into their raw-coordinate system.

Table 3
Simulated Single-exposure Catalog Parameters

Data Set	Δtime (yr)	Filter	Exposures	Δmag	Roll Angle	Scale (mas pixel^{-1})	X offset (pixel)	Y offset (pixel)
1	−1.78	*V*	5 long, 2 short	−0.1	130°	50	2100	1900
		I	5 long, 2 short	+0.1	−190°	50	2200	1800
2	0.0	*V*	5 long, 2 short	+0.05	20°	50	1900	2100
		I	5 long, 2 short	−0.5	85°	50	1800	2200
3	0.7	*V*	4 medium	+1.5	80°	28.27	500	500
		I	4 medium	+1.5	80°	28.27	500	500
4	+1.3	*I*	5 long, 2 short	−0.07	210°	40	2030	2020
5	+1.4	*V*	5 long, 2 short	+0.1	60°	40	2020	2030

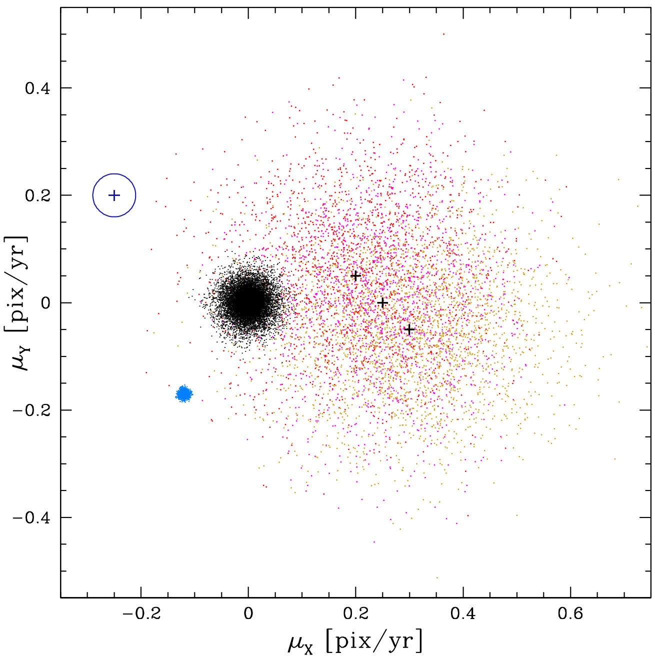

Figure 6. Vector point diagram of all of the population components of our comprehensive simulation, color-coded as in Figure 5. The GAL2 stars have zero PM dispersion, so they fall underneath the cross inside the blue circle. The means of the three field components are marked by black crosses.

(A color version of this figure is available in the online journal.)

Finally, to resemble positional uncertainties, an additional Gaussian-like shift in a random direction is added to each star's position (with a dispersion equal to its expected error; see Section 5.2). A similar method was used to introduce scatter in the magnitudes.

6.2.3. Results of the Full Simulation

We now have at our disposal single-exposure catalogs constructed as if they were the result of reduced images. We derived from them an output master frame using exposures of data set number 2 for positions and using all of the exposures for photometry. The recovered master frame is necessarily different from the input master frame: it contains uncertainties in the transformation parameters (because of the position shift added to each star related to its PM plus measurement error), and it has errors in the average position and errors in the magnitude of its stars. The recovered master frame CMD is shown on panel (a) of Figure 7. It contains only unsaturated stars. Stars measured in deep exposures have a magnitude value up to ∼−13.5, and brighter stars are measured only in short exposures.

Table 4
Measured Velocity Dispersions of Simulated GAL1 and GAL2 stars

Mag Range	GAL1 σ_μ (pixel yr^{-1})	GAL2 σ_μ (pixel yr^{-1})
(−12, −11)	0.0068	0.0029
(−11, −10)	0.0066	0.0034
(−10, −9)	0.0071	0.0048
(−9, −8)	0.0102	0.0062
(−8, −7)	0.0226	0.0087
(−7, −6)	0.0282	0.0252

The input master frame was not used beyond this. The recovered master frame was the one used to compute proper motions. For simplicity, hereafter we refer to the recovered master frame simply as the master frame.

Because of the different pointings and orientation of each data set, there will be master-frame stars present in some but not all of the exposures. As a consequence, the time baseline available for some stars will be shorter than 3.18 yr.

We treated our master frame as if it came from the official GO-10775 release and our simulated single-exposure catalogs as if they were the output of our reduction routines. We measured PMs in the exact same way that we do for real data sets. Panels (b1) to (b5) of Figure 7 show the recovered vector point diagrams for five different magnitude bins, highlighted by gray horizontal lines in panel (a), from the bright bin to the faint one, respectively.

As expected, the velocity dispersion of GAL1 stars is found to be larger than that of GAL2 stars (see, e.g., the different size of the GAL1 and GAL2 clouds of points in panels (b2) to (b5) of Figure 7). The one-dimensional velocity dispersion of GAL2 stars, i.e., the estimate of our internal errors, goes from ∼3 milli-pixel yr^{-1} at $V = -11.5$ to ∼25 milli-pixel yr^{-1} at $V = -6.5$. In the same magnitude interval, GAL1 stars have a measured velocity dispersion (i.e., without subtracting the error in quadrature) ranging from ∼7 milli-pixel yr^{-1} to ∼28 milli-pixel yr^{-1} and is systematically larger than that of GAL2 stars. Table 4 lists velocity–dispersion values for both galaxies in 6 mag ranges.

Panel (c) of Figure 7 illustrates the trend of PM errors as a function of the instrumental magnitude. We can distinguish two tails of errors at fainter magnitudes: a more-populated, smaller error trend, corresponding to stars with motions measured using the full 3.18 yr of time baseline, and a second, less-populated tail that corresponds to stars with a time baseline of 1.78 yr. Moreover, there is an increase in the PM errors for stars brighter than ∼−13.5 mag. These stars are measured only in the short

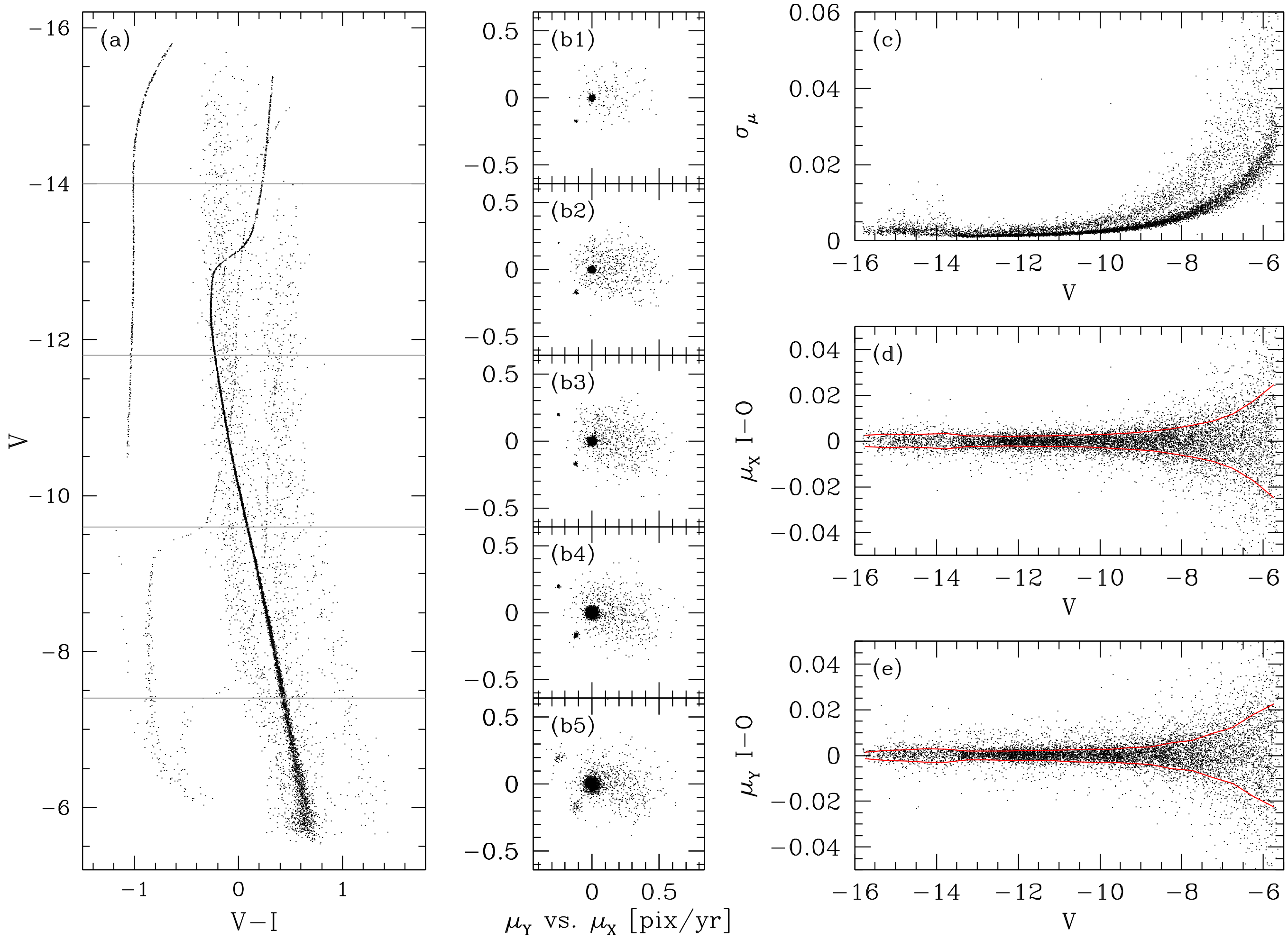

Figure 7. Results of our comprehensive data simulation. The recovered master-frame CMD is shown in panel (a). Proper motions are divided into 5 mag bins (gray horizontal lines) and displayed in panels (b1) to (b5), from the brighter to the fainter bin. Proper-motion errors as a function of the instrumental magnitude are shown in panel (c). The input−output difference of stellar PMs along the X and the Y axes, as a function of the instrumental magnitude, are shown in panels (d) and (e), respectively. Red lines in both panels mark the 68.27 percentile of the residuals around the median values.

(A color version of this figure is available in the online journal.)

exposures (eight out of 50), and therefore their PMs are less well constrained.

Panels (d) and (e) show the difference (defined as input−output, I−O) of each component of the motion. Red lines mark the ±68.27 percentile (rms) of the I–O values around the median values. These two plots provide another way to estimate the internal errors of our procedure. For the particular simulation we set up, the μ_X I−O rms is about 0.0032 pixel yr^{-1} (0.13 mas yr^{-1}) for the short-exposure regime, and it goes from 0.0022 pixel yr^{-1} (0.09 mas yr^{-1}) at $V = -13$ to 0.0024 pixel yr^{-1} (0.10 mas yr^{-1}) at $V = -10$ to 0.006 pixel yr^{-1} (0.24 mas yr^{-1}) at $V = -8$, reaching 0.02 pixel yr^{-1} (0.8 mas pixel^{-1}) at $V = -6$. The rms of μ_Y I−O has a similar behavior. These values are consistent with the velocity dispersion of GAL2 stars.

The comparison of input and output PMs shows that our PM measurement algorithms are highly reliable. There are astrophysical applications for which accurate error estimates are crucial. For instance, when we want to measure the intrinsic velocity dispersion of cluster stars, we have to subtract in quadrature the PM measurement errors from the observed dispersion. When the errors contribute a large fraction of the observed dispersion, a small over- or underestimate of the errors leads to biased results.

To test this, we compute the intrinsic velocity dispersion of cluster stars from the PM catalog (as done in van der Marel & Anderson 2010) and check whether it is in agreement with the input values. The top panel of Figure 8 shows the inferred velocity dispersions (in black, with error bars) as a function of the instrumental magnitude (0.4 mas yr^{-1} corresponds to 0.01 pixel yr^{-1}on the master frame). The real (input) velocity dispersion of cluster stars is represented by red open circles. The agreement between input and output velocity dispersions (bottom panel) shows an absence of clear systematic residuals, meaning that our quoted PM errors are accurate and reliable.

There is perhaps a marginal discrepancy (at the 1.2σ level) at the faint-end magnitude limit, where it seems that the PM errors have been slightly overestimated, with the result that the inferred velocity dispersion is lower than the input one. However, this should not come as a surprise. The input velocity dispersion of faint GC stars is 0.03 pixel yr^{-1}, and their measured PM error is almost as large (∼0.025 pixel yr^{-1}; see panel (c) of Figure 7). One should always be careful in trusting results that come from the quadrature difference of quantities of similar size, especially when one of the quantities is an error estimate. The fact that, even at the faint limit of our simulated measurements, input and output velocity dispersions are still quite consistent (at the 1.2σ level) is a further validation of our methodology.

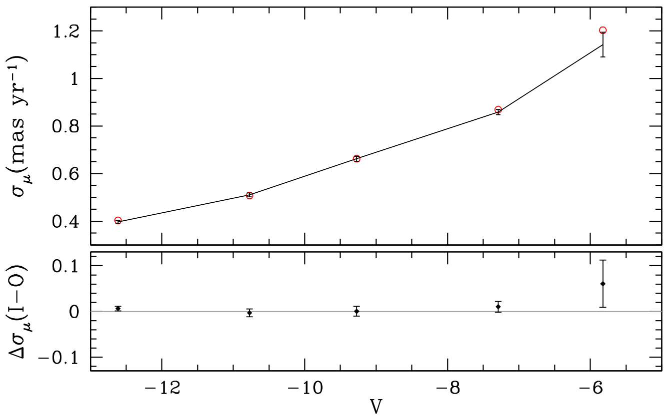

Figure 8. Top panel shows the input (red open circles) and inferred (black with error bars) velocity dispersion of cluster stars in our comprehensive simulation, as a function of the instrumental magnitude. The bottom panel shows the residuals between the input and the output values.

(A color version of this figure is available in the online journal.)

7. MITIGATING SOURCES OF SYSTEMATIC ERROR

In the previous section, we demonstrated that our PM-measurement algorithms are reliable when random errors and mild systematic effects are taken into account. Unfortunately, unaccounted for systematic sources of error may also be present in real data. In this section, we describe the methods we have adopted to mitigate their effects on our PM measurements.

In what follows, we will describe as an example the case of NGC 7078 (M 15). This is the cluster for which we will present the PM analysis and catalog in Section 8. NGC 7078 is a typical case among the 22 clusters in our study, in the sense that it has an average time baseline and an average number of data sets.

7.1. Chromatic Effects

A systematic effect that is always present in ground-based PM measurements is the so-called differential-chromatic refraction (DCR; see, e.g., Anderson et al. 2006; Bellini et al. 2009). The DCR effect shifts the photon positions on the CCD, and the displacement is proportional to the photon wavelength and to the zenithal distance of the observations. Space-based telescopes are obviously immune to DCR effects. Nonetheless, as anticipated in Section 3.3, we found a chromatic-dependent shift of blue and red stellar positions when UV filters are used with the WFC3/UVIS camera (Bellini et al. 2011), and for this reason we decided not to include observations taken with filters bluer than 330 nm.

A way to check whether or not our PM measurements are nonetheless affected by some chromatic-induced systematic effects is to analyze the behavior of the single components of the stellar motions as a function of the star colors. The left panel of Figure 9 shows the CMD of NGC 7078 around the HB and RGB regions. We selected stars in the magnitude range $15.7 < m_{\rm F606W} < 18$, in order to cover the largest available color baseline, and divided them into four color bins (blue, green, yellow, and red in the figure). The $\mu_\alpha \cos\delta$ component of their motions is shown in the top right panel, as a function of the star colors. We determined the median color and motion, with error, for each of the four groups of stars (black full squares). The same plot for the μ_δ component of the stellar motions is shown in the bottom right panel.

The median motions in each of the two right-hand panels are fitted with a weighted straight line (in black). Because we

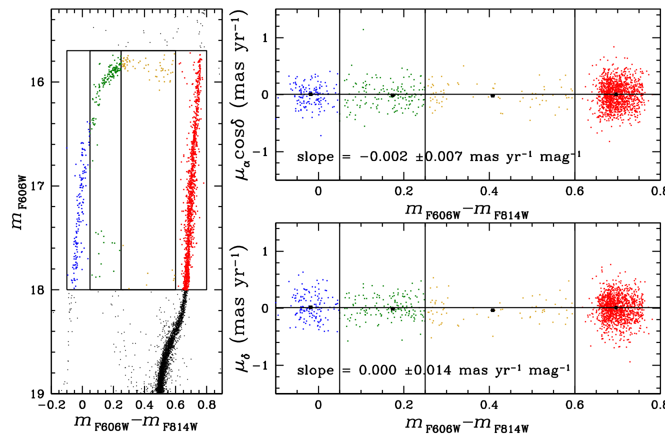

Figure 9. Left panel shows the CMD of NGC 7078 around the HB and RGB regions and the stars used to investigate the presence of chromatic-induced systematic effects. The right panels show the $\mu_\alpha \cos\delta$ and μ_δ components of the motion of selected stars as a function of the star colors (top and bottom panels, respectively). We divided and color-coded the selected stars into four groups according to their color, for clarity. We computed median motion and error for each group of stars and fitted two lines to the median points (the size of the errors are comparable to, or smaller than, the median points). The slopes of the fitted lines, consistent with zero, imply no chromatic-induced systematic errors in our measurements.

(A color version of this figure is available in the online journal.)

are using cluster members for the test, in principle the fitted lines should have no slope. On the other hand, slopes that significantly differ from zero would immediately reveal the possible presence of chromatic-induced sytematic effects. The computed slopes and errors are -0.002 ± 0.007 mas yr^{-1} mag^{-1} for $\mu_\alpha \cos\delta$ and 0.000 ± 0.014 mas yr^{-1} mag^{-1} for μ_δ. These values are consistent with zero well within their errors, and therefore we can rule out any presence of chromatic-induced systematic effects in our PMs.

7.2. CTE Effects

One problem not addressed by our simulations is that the GO-10775 master frame that was used for the real data is not really astrometrically flat. At the time the GO-10775 catalogs were released to the public, the pixel-based CTE correction for the ACS/WFC was not yet available. The stellar positions in the catalog thus suffer from this systematic error. As a result, single-exposure star positions transformed onto the master frame are affected by a systematic shift in position that is a function of both the location of the stars on the master frame and of their master-frame magnitude.

Our PM measurement algorithms produce as output the predicted position $(\overline{x}, \overline{y})$ of each star at the epoch of the master frame ($t = 0$), obtained as the intercept values of the least-squares fits versus time. This predicted position is based on a large number of (CTE-corrected) exposures, and not just those from GO-10775, and thus the new master frame should provide a better estimate of the true star position at $t = 0$. A comparison between the GO-10775 master-frame positions and the PM-based predicted positions $(\overline{x}, \overline{y})$ should therefore reveal the signature of uncorrected CTE effects in the GO-10775 master-catalog positions.

Panel (a) of Figure 10 shows the CMD of NGC 7078 for all of the stars in our PM catalog. We divided the CMD into 4 mag regions, from the brighter to the fainter, labeled R1 to R4. For each star in each magnitude region, we computed the 3σ clipped averaged difference (ΔX, ΔY) (in pixels) between the

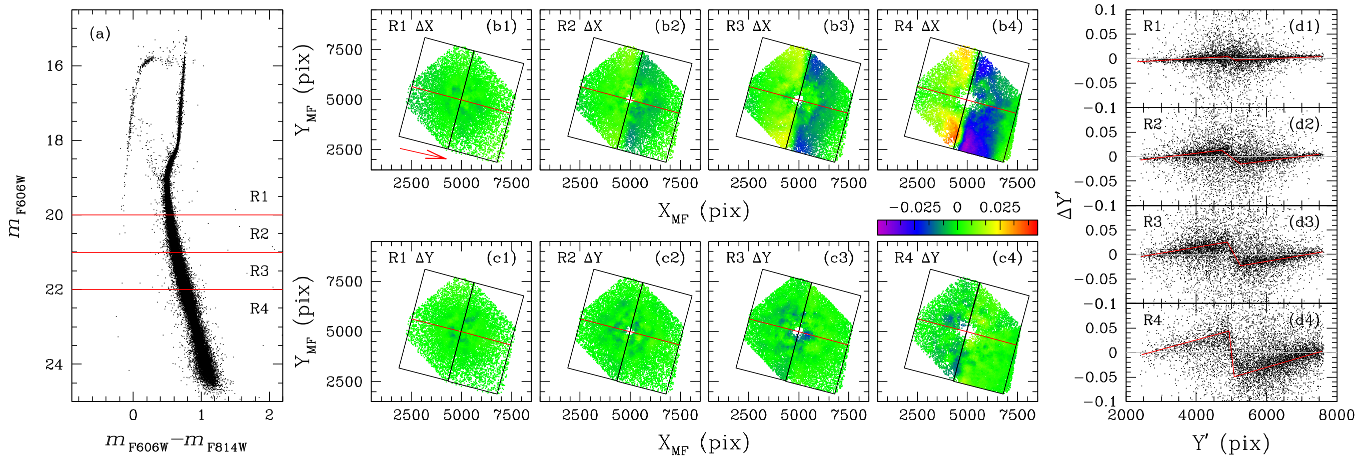

Figure 10. Effect of uncorrected CTE effects on the GO-10775 NGC 7078 master frame. Panel (a) shows the m_{F606W} vs. $m_{F606W} - m_{F814W}$ CMD. We divided the stars into 4 mag regions, labeled R1, R2, R3, and R4. For each region, we computed the locally averaged difference between the GO-10775 master-frame X and Y positions and those predicted by our PM fits at the epoch of the master frame. Panels (b1) to (b4) illustrate these differences for the X positions (ΔX) as a function of the stellar location on the master frame, for the magnitude regions R1 to R4. Panels (c1) to (c4) similarly show the differences in position along the Y axis (ΔY). Points are color-coded according to the size of the differences. A footprint of the typical location of the GO-10775 ACS/WFC chip placements is also shown in black, with individual amplifiers separated by a red line. A strong correlation between the pattern of position differences and the chip layout is evident. Panels (d1) to (d4) illustrate the position differences on a rotated reference system, such that the rotated Y′ axis is parallel to the raw Y direction of the GO-10775 exposures. The averaged ΔY′ residuals are highlighted by a red line. The fact that these residuals are strongly correlated with Y′ and increase at fainter magnitudes is a clear signature of unaccounted-for CTE losses.

(A color version of this figure is available in the online journal.)

master-frame and the PM-predicted positions, locally averaged over its surrounding 200 stars. Panels (b1) to (b4) show the map of the ΔX residuals for the magnitude regions R1 to R4, respectively. Panels (c1) to (c4) show the same for the ΔY residuals. Stars are colored according to the size of the residuals, following the color-coded bar on top of panel (c4). In each of these middle panels, we overplotted the typical GO-10775 layout, in which ACS/WFC single chips are drawn in black, and their amplifier subdivision is in red.

It is clear from panels (b) and (c) of Figure 10 that the pattern of residuals correlates with position on the master frame in the manner expected for a master frame not corrected for CTE losses.

CTE losses occur along the Y-axis direction of the raw GO-10775 exposures, highlighted by a red arrow in panel (b1). By rotating the master frame in such a way that its rotated Y axis Y′ is parallel to the raw Y axis of GO-10775, the position residuals ΔY′ directly reveal the impact of CTE losses. Panels (d1) to (d4) of Figure 10 show the ΔY′ residuals as a function of the Y′ position for the 4 mag regions. The red line in each panel indicates the average residual trend. The results are remarkably similar to, e.g., Figure 15 of Anderson & Bedin (2010) and leave no doubt that the source of the systematic error is CTE losses.

To mitigate the effect of uncorrected CTE losses on the master-frame positions, we remeasured all stellar PMs using the $(\overline{x}, \overline{y})$ values as the new master-frame positions. Figure 11 shows the ΔY′ residuals (not binned in magnitude) as a function of the Y′ positions, obtained by using the original GO-10775 master frame (in black) and the improved master frame (in red). This figure clearly shows that our procedure successfully eliminates most of the impact of uncorrected CTE losses in the GO-10775 master-frame positions. We therefore used this procedure for all final PM calculations.

7.3. Other Residual Systematics

Even in the ideal case of a systematics-free master frame, imperfectly corrected geometric distortion and CTE residuals

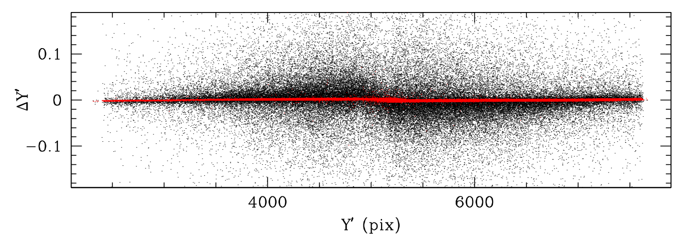

Figure 11. Rotated ΔY′ position offsets as a function of the Y′ position using the original GO-10775 positions as the master frame (black, same as panel (d) of Figure 10, but not binned in magnitude) and using the PM-predicted positions at $t = 0$ (red). The latter are used for all of our final PM catalogs.

(A color version of this figure is available in the online journal.)

are always to be expected in our single-exposure star positions. Depending on how a given data set is oriented and dithered with respect to the master frame, these uncorrected residuals may affect the measured PMs.

To assess the extent of any remaining systematic effects in our catalogs, we considered two-dimensional maps of the mean PM of cluster stars. To the lowest order, no mean PM is expected. In the radial direction, any contraction or expansion due to core collapse or gravothermal oscillations is too slow to induce measurable PMs. The same is true for any apparent contraction or expansion due to a cluster's line-of-sight motion away from or toward us. In the azimuthal direction, there may, in principle, be nonzero mean PMs due to cluster rotation. However, clusters are generally close to spherical, so any rotation is expected to be small. Moreover, our calibration procedure, using six-parameter linear transformations to align frames, removes any inherent solid-body rotation component from the mean PM field (see discussion in van der Marel & Anderson 2010). Therefore, the only mean PM components that may in principle be present in our PM catalogs are small differential-rotation components. Such components should be azimuthally aligned with a well-defined symmetry around the cluster center. Any other mean

Table 5
Amplifier-based, Local Average PM Statistical Quantities

Unit	Minimum	Median	Maximum	Semi-inter.
		$\mu_\alpha \cos\delta$		
pixel yr^{-1}	−0.0049	0.0003	0.0079	0.0011
mas yr^{-1}	−0.2017	0.0119	0.3143	0.0444
km s^{-1}	−9.9487	0.5867	15.495	2.1914
km s$^{-1}/\sigma_{V_{\rm LOS}}$	−0.7368	0.0405	1.1478	0.1623
		μ_δ		
pixel yr^{-1}	−0.0042	0.0003	0.0049	0.0008
mas yr^{-1}	−0.1737	0.0111	0.1948	0.0322
km s^{-1}	−8.5683	0.5472	9.6037	1.5875
km s$^{-1}/\sigma_{V_{\rm LOS}}$	−0.6346	0.0405	0.7114	0.1176

Table 6
Locally Corrected, Local Average PM Statistical Quantities

Unit	Minimum	Median	Maximum	Semi-inter.
		$\mu_\alpha \cos\delta$		
pixel yr^{-1}	−0.0024	0.0000	0.0028	0.0004
mas yr^{-1}	−0.0992	0.0007	0.1100	0.0149
km s^{-1}	−4.8954	0.0345	5.4230	0.7345
km s$^{-1}/\sigma_{V_{\rm LOS}}$	−0.3625	0.0026	0.4017	0.0544
		μ_δ		
pixel yr^{-1}	−0.0026	0.0000	0.0027	0.0004
mas yr^{-1}	−0.1063	0.0010	0.1063	0.0151
km s^{-1}	−5.2454	0.0493	5.2406	0.7444
km s$^{-1}/\sigma_{V_{\rm LOS}}$	−0.3885	0.0037	0.3882	0.0551

PM component inherent in our catalogs is therefore a likely indication of residual systematic errors.

We constructed a two-dimensional (2D) map for each component of the average motion by color-coding each star in our NGC 7078 PM catalog according to the average motion of its surrounding 200 stars. We used 3σ clipping to remove any influence from noncluster members. The top panels of Figure 12 show the so-derived 2D maps for the X (left) and the Y (right) components of the motion. The color scale is shown in the top-right panel of the figure, in units of pixel yr^{-1}. The panels reveal the presence of systematic errors. Transitions between lower and higher average PM values happen in proximity to the detector or amplifier edges of the adopted data sets, namely: GO-10401, GO-10775, GO-11233, and GO-12605 (see Table 27 for the full list of exposures we used). To quantify the size of these systematic trends, we computed for each component of the locally averaged motion the minimum, median, maximum, and semi-interquartile values in four different PM units: mas yr^{-1}, pixel yr^{-1}, km s^{-1} and km s$^{-1}/\sigma_{V_{\rm LOS}}$, where $\sigma_{V_{\rm LOS}}$ is from Table 1. Table 5 collects these values.

In an absolute sense, the systematic trends are generally very small. In fact, 50% of the stars in our catalog have locally averaged PMs smaller than 0.0011 and 0.0004 pixel yr^{-1} for the X and the Y components, respectively. As a reference, we recall that we can measure the position of bright, unsaturated stars in each exposure with an average precision of ~0.01 pixel. Nevertheless, there are locations on the master frame where the systematic trends are as large as ~0.008 pixel yr^{-1}. The available time baseline for these locations is about 5.5 yr, giving a total displacement of more than 0.04 pixels.

These systematic trends have the potential to significantly affect specific scientific studies. Even though the systematic trends are typically only as large as ~15% of the quoted velocity dispersion $\sigma_{V_{\rm LOS}}$ (at least for NGC 7078), there are locations on the master frame where the systematic effects are even larger than $\sigma_{V_{\rm LOS}}$, so this may affect dynamical studies of the spatially dependent kinematics. In contrast, other scientific studies, e.g., those focusing on differences in kinematics between different subpopulations of the cluster, won't be affected by these systematic trends. The PM of stars of different populations will be locally biased in the same way.

The user of the catalogs can decide to simply not include stars in any high-mean PM regions in the analysis, but it can be tricky to carefully choose which stars are good and which stars are not. The choice depends on the specific scientific needs. In order to make our PM catalogs useful for a wide range of scientific investigations, the PMs in our catalogs are offered in two ways: the amplifier-based PM measurements discussed so far, and the locally corrected PM measurements obtained as described in the following section.

7.4. Local Corrections

Local PM corrections can be obtained in two ways: (1) a priori, by using a local sample of reference stars to compute the linear transformations from each single-exposure catalog onto the master frame (the so-called local-transformation approach; see, e.g., Anderson et al. 2006; Bellini et al. 2009); or (2) a posteriori, by locally correcting the PM of each star by the net motion of its surrounding neighbors. Our adopted local PM correction is of the latter kind.

Surrounding neighbors are chosen as follows. For each star in the PM catalog, we identify surrounding cluster stars within 600 pixels and within ±0.5 $m_{\rm F606W}$ magnitudes from the target star (to mitigate the effect of both uncorrected geometric distortion and uncorrected CTE residuals). Then, we compute the 3.5σ clipped median value of each component of the motion for these neighbors: $\overline{\mu_\alpha \cos\delta}$ and $\overline{\mu_\delta}$. We correct the motion of the target star by subtracting these values. If there are less than 50 neighbor stars, no correction is applied. If there are more than 150 neighbor stars, we compute $\overline{\mu_\alpha \cos\delta}$ and $\overline{\mu_\delta}$ values using only the closest 150 stars.

Panels (c) and (d) of Figure 12 show the locally averaged PMs after our local correction is applied. Points are color-coded in the same way as for the amplifier-based average motions. As expected, all systematic spatial PM trends have been removed. Table 6 collects the same statistical quantities as Table 5, but now for the local-corrected PMs. The improvement offered by the local correction with respect to the amplifier-based PMs is evident in all values listed in Table 6.

Because uncorrected CTE residuals are a function of both stellar positions and magnitudes, a further proof that our local corrections are able to properly remove any systematic-error residual would be the absence of trends in the PM versus magnitude plane. The two panels of Figure 13 show each component of the locally corrected PMs as a function of the stellar magnitude. We computed 3.5σ clipped median motions and errors binning every 0.5 mag (red points; error bars are comparable to, or smaller than, the median points). Rejected points are marked with gray crosses. The red horizontal lines indicate the absence of any systematic trend and are not a fit to the points, which all lie on the lines well within their errors.

It is clear from Figures 12 and 13 that locally corrected proper motions successfully correct any spatially and magnitude-dependent systematic trends. However, users should carefully

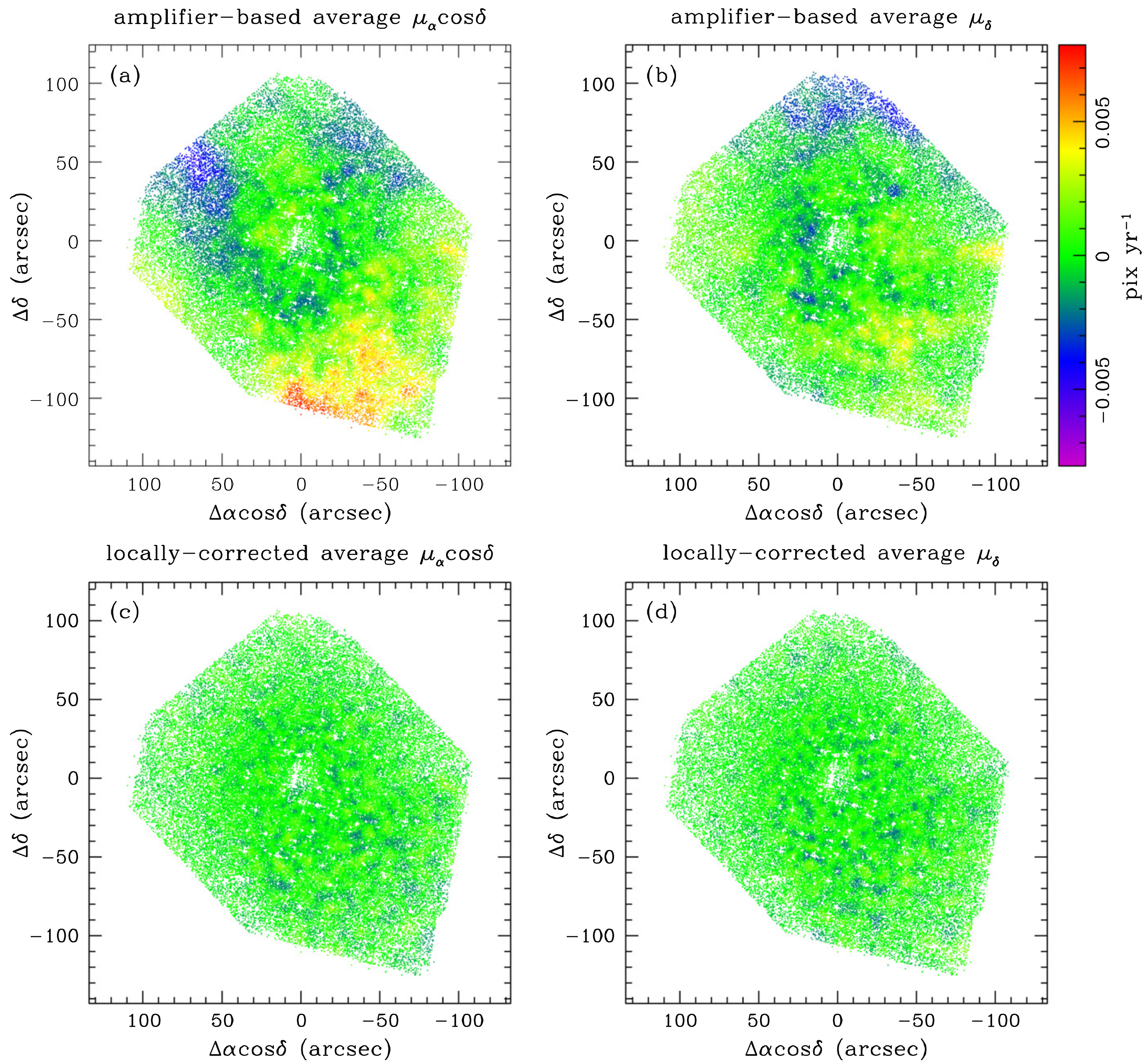

Figure 12. Top panels show two-dimensional maps of the locally averaged $\mu_\alpha \cos\delta$ (a) and μ_δ (b) components of the PM, as a function of positions with respect to the cluster center (in units of arcsec). Stars are color-coded according to their locally averaged PM, according to the color bar on the top right. Bottom panels show the same after we applied our local correction described in Section 7.4.

(A color version of this figure is available in the online journal.)

consider whether it is best to use the amplifier-based PMs or the locally corrected PMs. The latter have fewer systematics, so they may be best for studies of, e.g., cluster velocity dispersion profiles. However, locally corrected PMs have any intrinsic mean motion removed by brute force. Therefore, they are not suitable for studies of, e.g., cluster rotation.

7.5. Selections Based on Data-quality Parameters

In the previous sections, we discussed systematic effects that affect all of our PM catalogs. Other sources of systematic errors, e.g., those caused by crowding, affect some clusters more than others. Moreover, such systematics are relevant to only some of the scientific investigations listed in the Introduction (e.g., internal motions). As part of the PM analysis, we derive several data quality parameters that are reported in our catalogs. These parameters can serve as diagnostics to determine which stars to include or exclude from a particular analysis, depending on the specific scientific needs.

We do not include in our catalogs stars with obvious neighbors (see Section 4). Nonetheless, some stars in our catalogs will be affected by (faint) neighbors, even when not explicitly recognized as such. The resulting crowding-induced systematic effects are among the most subtle sources of error. In clusters with a very dense core, the measured position of sources with neighbors is shifted away from its true position. This causes a systematic PM error if the shift is not the same at different epochs. This can happen if the sources have a high relative motion or if the sources are observed with different filters at

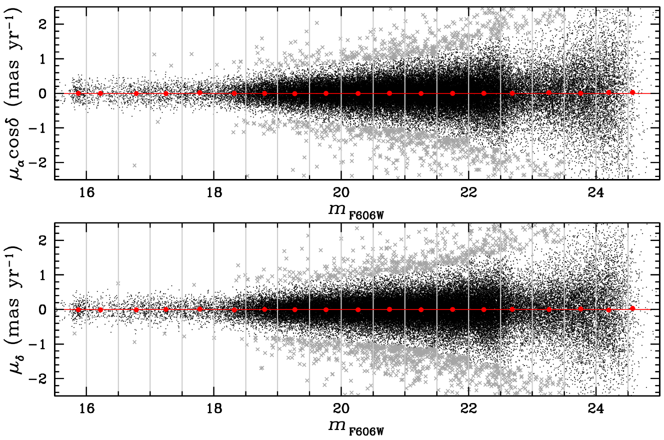

Figure 13. PM components as a function of the $m_{\rm F606W}$ magnitude: $\mu_\alpha \cos\delta$ (top) and μ_δ (bottom). Motions are divided into magnitude bins, and their 3.5σ clipped medians are shown in red, for each bin. The sizes of the median errors are comparable to, or even smaller than, the median points. Rejected points are marked with gray crosses. The red horizontal line shows the absence of any magnitude trend and is not a fit to the points.

(A color version of this figure is available in the online journal.)

different epochs. To illustrate the latter case, consider the case of two close sources: a red and a blue star. When observed through a red filter, the apparent shift induced by one star on the position of the other is different than when observed through a blue filter. If we have only two epochs of observations, one based on red and one based on blue exposures, then this will induce systematic PM errors. The situation is obviously worse the closer the stars are (and especially when dealing with complete blends) or when there are multiple close neighbors of different colors.

The `QFIT` parameter included in the GO-10775 catalogs (which is also replicated in our PM catalogs) is an important diagnostic to assess crowding effects. This parameter quantifies how well a source has been fit with the PSF model. This, in turn, correlates with the amount of light contamination from neighbor stars that fell within the region over which the stellar profile was fitted. Lower `QFIT` values correspond to more isolated, less systematicly affected stars.

Another parameter that helps in assessing crowding effects on the PM measurements is the reduced χ^2. For position measurements with only Gaussian random errors, the least-squares linear fits, we used to measure PMs should generate $\chi^2 \approx N$, where N is the number of degrees of freedom. Hence, it should result in a reduced $\chi^2 \approx 1$. Instead, when the position measurements also contain systematic errors, the reduced χ^2 tends to be larger. Rejecting stars with large `QFIT` or large reduced χ^2 values therefore helps to minimize the effect of crowding-induced systematics on the PM catalog.

A third diagnostic worth mentioning is N_R, defined as the ratio $N_{\rm used}/N_{\rm found}$. Here, $\mathrm{N}_{\rm found}$ is the total number of data points initially available for the PM straight-line fits, and $\mathrm{N}_{\rm used}$ is the final number of data points actually used after the one-point-at-a-time rejection algorithm (see Section 5.5). If N_R is low, then a high fraction of data points are rejected in the PM fit of a given star, and one should be suspicious about the quality of the resulting PM measurement.

As a practical example, let us again consider NGC 7078. Because this is a post-core-collapse cluster, its level of crowding is very high even at *HST* resolution. Therefore, crowding- or blending-driven systematics are expected to play an important role. When two stars on the MS are blended, their blended sum typically shows up as a source on the red side of the MS (this is because the fainter star that perturbsthe brighter star is redder, owing to the MS slope in the CMD). So to look for a possible signature of systematic PM errors, we studied in NGC 7078 the dependence of the PM kinematics as a function of color within a given magnitude range.

We selected NGC 7078 stars along the MS in the magnitude interval $19 < m_{\rm F814W} < 21$ (panel (a) of Figure 14). We drew by hand two fiducial lines on the blue and on the red side of the MS (in red in the panel) and used them to rectifythe MS so that the blue-side and red-side fiducials have a Δ^N color of zero and one, respectively, on the rectified plane (panel b). We then defined three subsamples of stars: the blue MS (bMS, in blue), the red MS (rMS, in red), and a sample containing very red objects (vrO, in green). The vrO sample should contain mostly blends because the binary fraction of NGC 7078 is less than 4% (Milone et al. 2012) and the photometry is corrected for differential reddening. The velocity–dispersion profiles for the three PM subsamples (determined as described in Section 8.3 below) are shown as a function of the radial distance in panel (c).

It is evident that the velocity dispersion is systematically higher for redder stars. This can be explained by assuming that

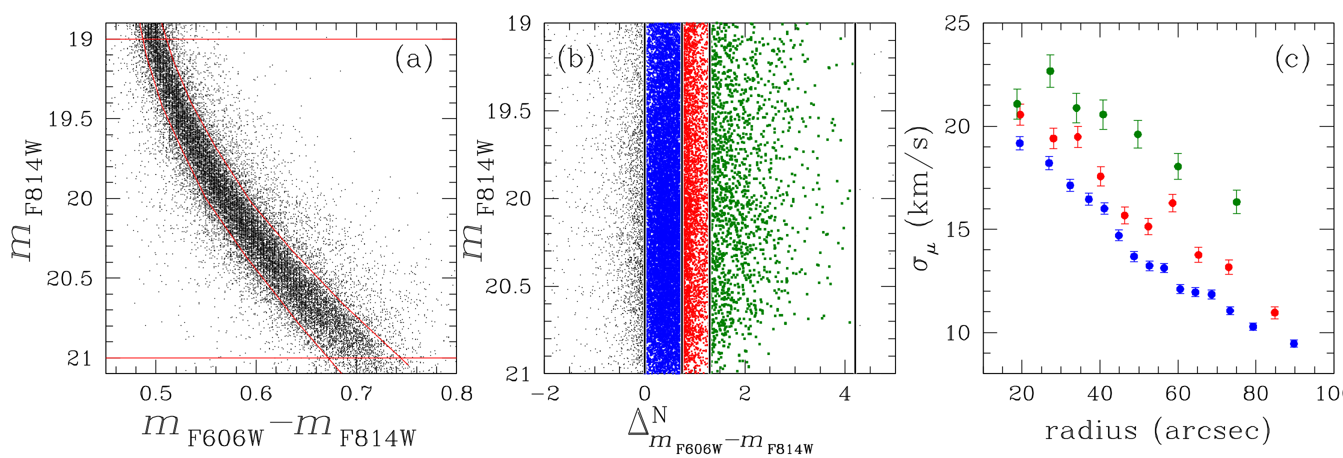

Figure 14. Panel (a): the upper MS of NGC 7078. Stars in the magnitude range $19 < m_{\rm F814W} < 21$ (horizontal red lines) are selected for measurement of the velocity dispersion. The two red lines along the MS are used for the rectification of MS stars shown in panel (b), where we define three samples of stars according to their color: bMS (blue), rMS (red), and very red objects (vrO, in green). The radial velocity–dispersion profile of the three components is shown in panel (c), where we can see the effects of crowding or blending on σ_μ, as described in the text.

(A color version of this figure is available in the online journal.)

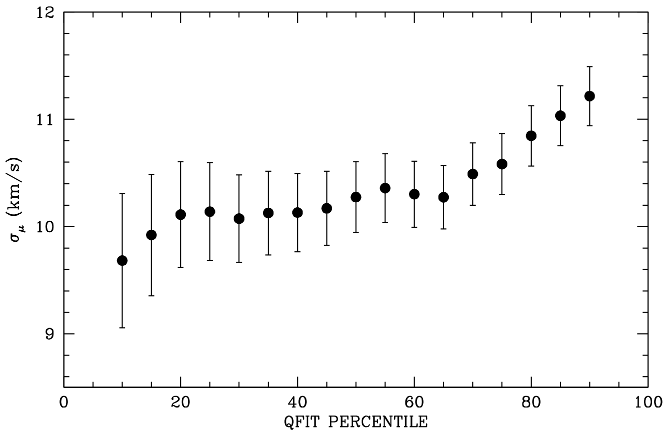

Figure 15. Sensitivity of the inferred velocity dispersion of NGC 7078 stars with similar kinematic properties to different QFIT selection cuts on the PM catalog. NGC 7078 is the prototype of high-central-density clusters with unbalanced filters in the different epochs, for which use of appropriate cuts based on data quality parameters is important.

the redder stars are affected by blending and that this blending induces a systematic component of PM scatter that is observed in addition to the actual random motions of the stars in the cluster. To test this hypothesis, one can repeat the analysis using only stars with smaller values of QFIT and reduced χ^2 and higher N_R. One would expect this to reduce the difference in velocity dispersion between the bMS, rMS, and vrO stars.

Choosing the optimal cuts for the QFIT, reduced χ^2, and N_R selections is a delicate issue. In principle, one can use an iterative approach in which one gradually rejects stars using increasingly stringent cuts and then measures the velocity dispersion for each progressive cut. Convergence in the measured velocity dispersions might occur if at some cut level all blended sources have been removed from the sample. In practice, though, the selections (especially those based on QFIT and reduced χ^2) preferentially remove fainter stars close to the cluster center, and these stars have intrinsically a higher velocity dispersion than other stars because of hydrostatic equilibrium and energy equipartition. This means that every time a sharper cut is applied to the sample, a counteracting bias is also applied to the surviving sample of stars. Hence, there may be no convergence in the inferred velocity dispersions as stronger cuts are applied.

For these reasons, the best way to choose cuts without introducing excessive selection biases is to select stars of similar luminosity (e.g., mass) and distance from the cluster center. As an example, we selected NGC 7078 stars in an annulus between 60 and 70 arcsec from the cluster center and between $m_{\rm F606W} = 20.3$ and 20.6 (about 1 mag below the turnoff).[18] We chose fixed cuts for the reduced χ^2 (<1.25) and N_R (>0.85) and applied various QFIT cuts to show how this affects the measured velocity dispersion. The initial total number of selected stars is 510. We measured the stellar velocity dispersion σ_μ by keeping the best 90, 85, 80, ..., 10 percentile of the QFIT values in both the $m_{\rm F606W}$ and $m_{\rm F814W}$ magnitudes.

Figure 15 shows the velocity dispersions thus derived for different QFIT cuts. Stars with high QFIT values are those with a higher chance of being affected by crowding or blending effects. As expected, going from right to left in the figure, more stringent QFIT cuts produce a smaller velocity dispersion for the surviving sample. Below the 65th percentile, the velocity dispersions converge and stay constant to within the errors. From this we infer that a 65th percentile cut is able to remove most of the blended objects from the sample. The small decrease of σ_μ as a function of the QFIT below the 65th percentile is likely due to the fact that even in the small magnitude and radial range under consideration, progressively stronger cuts induce a kinematic bias in the surviving sample, as described above.

Based on these considerations, we reanalyzed the bMS, rMS, and vrO samples of NGC 7078 as in Figure 14, but now including only stars that have $\chi^2 < 1.25$ and $N_R > 0.85$ and survive a 50th percentile QFIT cut. The results are shown in Figure 16. The velocity dispersions of the three MS components are now comparable. This supports the hypothesis that the kinematic differences evident in Figure 14(c) were entirely due to blending-induced PM systematics. It also supports the notion that the cuts applied here are necessary and sufficient for this particular PM catalog. It should be noted that even for the bMS stars, for which the observed color provides no indication of blending, the velocity dispersion drops significantly after application of the cuts. Therefore, for dynamical studies of clusters such as NGC 7078, it is critical to use the data quality parameters provided in our catalogs to compose an optimal sample. This is due to the combination of several effects,

[18] If we were to use stars that are fainter or closer to the center, then low-number statistics would have become a problem.

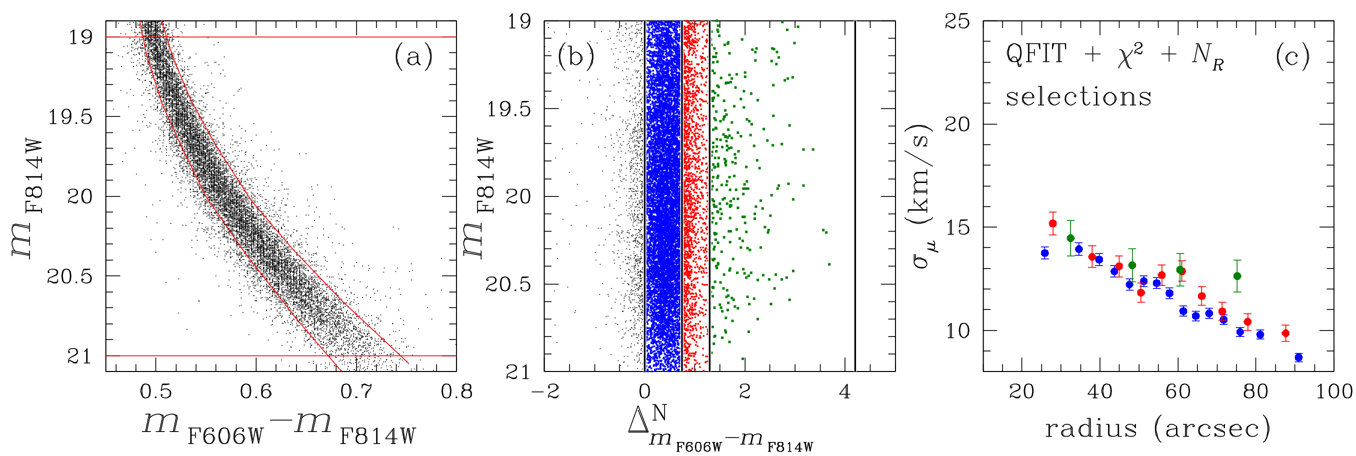

Figure 16. Similar to Figure 14, but for the subset of NGC 7078 catalog stars with high-quality PMs. There is now no disagreement between the velocity dispersions of the three MS samples in panel (c), and the σ_μ values are reduced across the board compared to Figure 14.

(A color version of this figure is available in the online journal.)

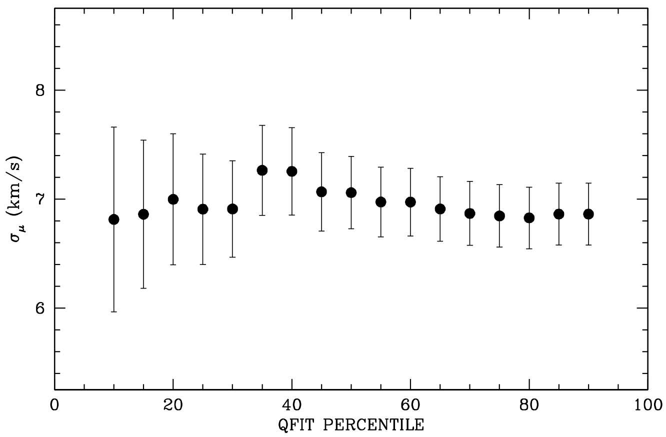

Figure 17. Similar to Figure 15, but for NGC 6752, a closer and less massive cluster and with a more homogeneous filter or epoch coverage than NGC 7078. In this case, cuts based on data quality parameters do not significantly affect the inferred velocity dispersion.

including the fact that NGC 7078 is post-core-collapse, the fact that it is relatively distant, the fact that we only have a few epochs of data for this cluster, and the fact that the data at different epochs were taken in different filters. Faint stars and stars at small radii are the most sensitive to these effects because they tend to be most affected by crowding.

Other less-crowded clusters, or clusters for which a large number of exposures are available (even when taken through a variety of different filters), are far less affected by crowding- or blending-induced PM systematics. As an example, we repeated the same selection test shown in Figure 15 on the PM catalog of NGC 6752. This cluster has nearly 300 exposures of its core taken with nine different filters spanning from F390W to F814W (see Table 25), and it is much closer than NGC 7078 (4.0 kpc instead of 10.4). The test was performed on MS stars with magnitudes $18.3 < m_{\rm F606W} < 18.6$ (about 1 mag below the turnoff) and between 50 and 60 arcsec from the cluster center. Figure 17 shows the results of this second test. In this case, the measured velocity dispersions all agree within the uncertainties, regardless of the applied `QFIT` cut.

7.6. Caveats

In Section 6, we showed that the techniques we developed to measure high-precision PMs with the *HST* are highly reliable, and our PM errors are a very good representation of the true errors. In this section, we showed that we are able to identify and correct systematic errors introduced by the use of nonoptimal master frames (Section 7.2), by uncorrected geometric distortion and uncorrected CTE residuals in the single-exposure catalogs (Sections 7.3 and Section 7.4), and by crowding and blending (Section 7.5). We believe that with the corrections described in these sections, our PM measurements are as good as they can be, given the limitations of the data available in the *HST* archive (which are extremely heterogeneous and were rarely obtained for the purpose of astrometry). Nevertheless, several more issues need to be kept in mind when using our PM catalogs.

Our catalogs are necessarily incomplete, and in different ways for different clusters. For instance, in the most-crowded central regions of each cluster, we can measure PMs for only the brightest stars. Specific dynamical studies, like the search for intermediate-mass black holes, require a large number of stars with high-quality PMs in the very proximity of the cluster center. This does not mean that our PM catalogs are not suitable for these kinds of studies in general, but some clusters will be more appropriate than others, and it depends on the crowding conditions of their centers. A better way to measure high-quality PMs for a large number of stars in the cluster centers would be to have used a master frame based on higher spatial resolution ACS/HRC exposures (when available) rather than on the ACS/WFC data, but this goes beyond the scope of the present work.

We saw in Section 6.2.3 that at the faint limit, there might be some nonnegligible systematic errors in the measured velocity dispersion. Estimation of the velocity dispersion requires, in essence, that the PM-measurement uncertainties be subtracted in quadrature from the observed PM scatter. At the faint end, the PM uncertainties become comparable to (or exceed) the velocity dispersion of the cluster. Very accurate estimates of the PM-measurement uncertainties are then required in order to obtain reliable results. In our somewhat idealized simulations of Figure 8, PM uncertainties can be fairly reliably estimated at all magnitudes. In practice, there is always the potential of low-level unidentified systematic errors. The random errors estimated by our algorithms are then at best only an approximation to the true uncertainties. For this reason, it is advised to restrict any dynamical analysis to stars for which the PM uncertainties are well below the cluster velocity dispersion. This is particularly important for studies of energy equipartition (e.g., Anderson & van der Marel 2010; Trenti & van der Marel 2013), which rely on quantifying the increase of the velocity dispersion with decreasing stellar mass. It is then particularly important to reliably understand how the PM-measurement errors increase toward fainter magnitudes.

The errors in our catalogs are not homogeneously distributed. Some locations of the master frame will have larger time baselines or more single-exposure measurements. Taking special care in selecting high-quality PMs is therefore always crucialand a delicate matterregardless of the specific scientific needs (unless PMs are only used to select a cleaned sample of cluster stars for photometric studies).

8. PROPER-MOTION KINEMATICS OF NGC 7078

Our PM catalog for NGC 7078 is described in Appendix B and is distributed electronically as part of this paper (Table 30).

8.1. Overview

Figure 18 provides a visual overview of the information contained in the catalog. Panel (a) shows the GO-10775 CMD, corrected for differential reddening, for all stars with a PM measurement. We measured PMs from just above the HB region down to ∼5 mag below the MS turnoff. The total spatial coverage of the catalog is shown in panel (b), with respect to the cluster center. We added two circles of radius 1′ and 2′ for reference. The histogram of the time baseline used to compute each star's motion is shown in panel (c). The Y axis of the plot is in logarithmic units, to properly show all histogram bins using the same scale. Panel (d) shows the PM vector point diagram, in units of mas yr^{-1}. Histograms of the PM distribution for each component of the motion and for each time baseline bin are also shown, again on a logarithmic Y-axis scale. Finally, PM errors as a function of the $m_{\rm F606W}$ magnitude are shown in panel (e). In each panel, stars are color-coded according to their time baseline. The figure gives an immediate sense of the PM distribution, quality, and respective magnitude range in each location of the available FoV. Proper motion errors are smaller than 30 μas yr^{-1} for the brightest stars with the longest time

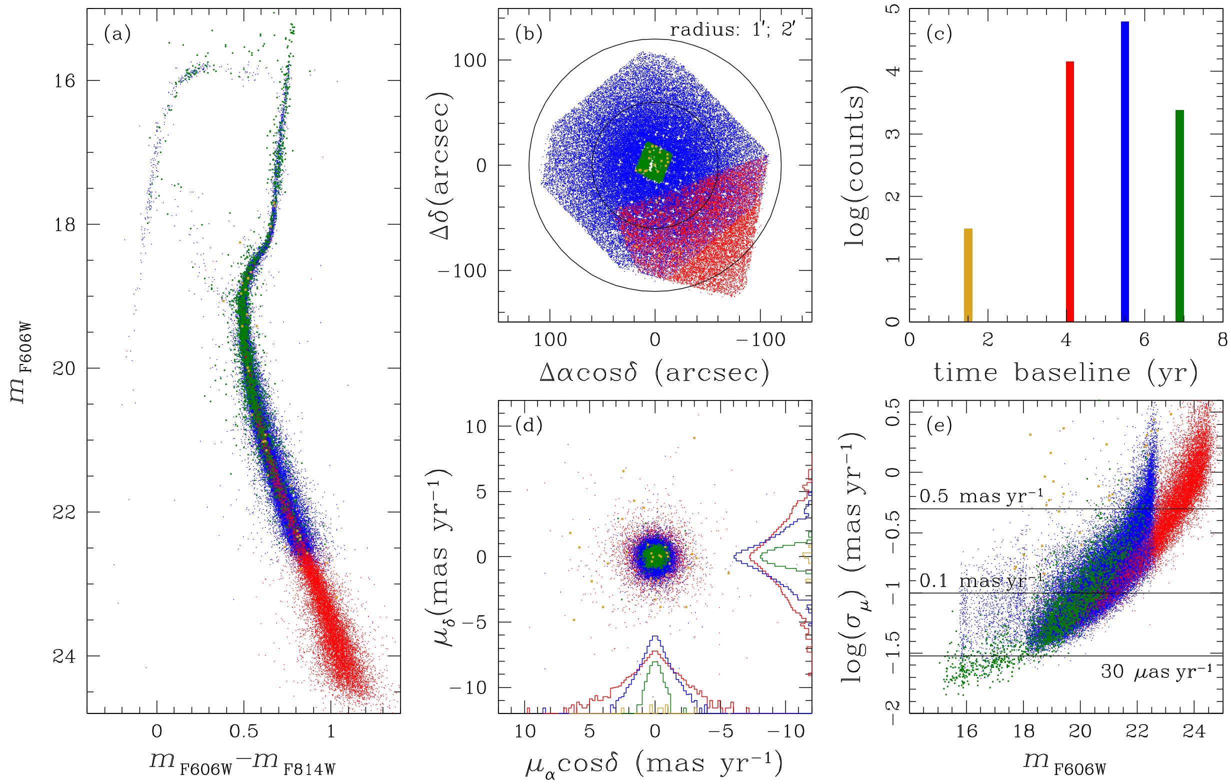

Figure 18. Panel (a): the CMD of all stars in the NGC 7078 PM catalog. Panel (b): stellar spatial distribution with respect to the cluster center, in arcsec. Two circles at 1′ and 2′ are shown for reference. Panel (c): logarithmic histogram of the time baseline used to compute PMs. The counts refer to the number of stars. Panel (d): PM diagram, together with histograms of the two PM components for each available time baseline. Panel (e): PM errors as a function of the m_{F606W} magnitude. In each panel, stars are color-coded according to their time baseline.

(A color version of this figure is available in the online journal.)

baseline and increase up to ∼3 mas yr^{-1} for the faintest stars in the catalog. There are 32 stars in the catalog with a time baseline of less than 2 yr. Although the PM of these stars is poorly constrained, they are included in the catalog for completeness.

8.2. Comparison with Other Published PM Catalogs

The internal PM dispersion of NGC 7078, based on 210 bright RGB stars, was first (barely) detected by Cudworth (1976), using photographic plates spanning over 70 yr of time baseline. The first high-quality PM catalog of NGC 7078 was published by McNamara et al. (2003, hereafter McN03) for 1764 stars in the core, obtained with the *HST* WFPC2 detector. The authors computed proper motions using four first-epoch and 12 s epoch exposures taken ∼8 yr apart. Their catalog includes positions in the geometric-distortion-corrected frame of their first exposure, in pixels, and proper motions as displacements in pixels over the available time baseline.[19]

We applied general six-parameter linear transformations to translate the McN03 WFPC2 positions into our master frame and cross-identified their stars with the closest stars in our catalog within 2.5 pixels. A total of 686 stars were found in common, 323 of which were used in their internal PM analysis. Among them, there are 26 stars in the proximity of McN03 FoV edges that exhibit a significant offset in position with respect to our master frame, probably due to unaccounted for WFPC2 geometric distortion residuals. These 26 stars are not included

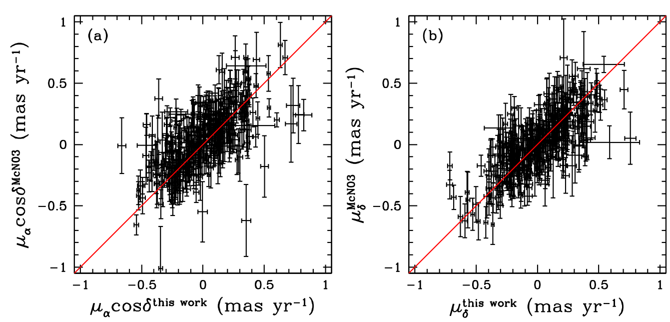

Figure 19. PM component-to-component comparison between our catalog and that of McN03. Most of the scatter is due to the larger error bars of the McN03 catalog.

(A color version of this figure is available in the online journal.)

in the PM comparison. Finally, we transformed quoted McN03 PMs and errors into ($\mu_\alpha \cos\delta$, μ_δ) units.[20]

In Figure 19, we illustrate the comparison between our PMs and those of McN03, with $\mu_\alpha \cos\delta$ in panel (a) and μ_δ in panel (b). Most of the scatter is due to the uncertainties of the McN03 PM measurements, which are significantly larger than those in our catalog (our catalog is also superior in that it has 40 times as many stars). The fact that the points are mostly aligned along the red line implies that our PMs are consistent with those of McN03. The scatter of the points along the direction

[19] Note that McN03 quoted displacements are to be intended as first-epoch positions minus second-epoch positions and not vice versa.

[20] In order to convert McN03-quoted PMs into mas yr^{-1} units, we applied a scaling factor of 5.69 instead of their suggested 5.75 (a 1% difference). This difference is due to the different pixel scale adopted for WFPC2: they use a 46 mas pixel^{-1} scale value, while we directly measured their plate scale on our master frame to be 45.46 mas pixel^{-1}.

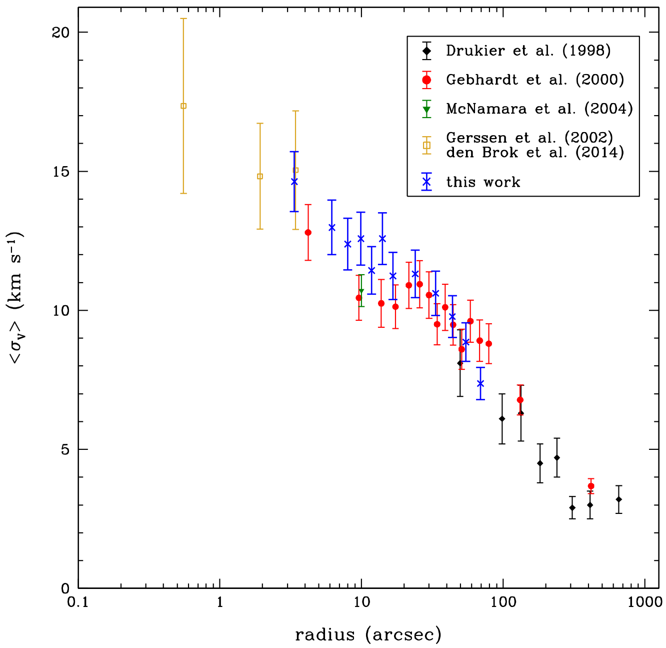

Figure 20. Velocity–dispersion profiles in the literature (black, red, and green points) and that obtained with RGB stars in our catalog (in blue), assuming a cluster distance of 10.4 kpc (see Table 1).

(A color version of this figure is available in the online journal.)

perpendicular to the red line (which is not a fit to the data but just the plane bisector) reveals a small but marginal (within the errors) disagreement. The fact that our PMs are consistent with those of McN03 is a further indication of the reliability of our measurements.

8.3. *Velocity–dispersion Profiles*

In 1989, Peterson et al. (1989) first measured the line-of-sight velocity–dispersion profile of NGC 7078, based on 120 spectra of individual stars in the centermost 4′.6. In subsequent years, many authors have analyzed the line-of-sight velocity–dispersion profile of NGC 7078 with various telescopes and techniques. High signal-to-noise spectra are generally obtained from only the brightest stars in a GC (i.e., RGB stars). In Figure 20, we therefore compare literature high-quality velocity–dispersion profiles (in black, red, green, and yellow for Drukier et al. 1998, Gebhardt et al. 2000, McNamara et al. 2004, and Gerssen et al. 2002/den Brok et al. 2014, respectively[21]) with that obtained from the stars in our catalog brighter than the SGB (in blue), using 10.4 kpc as the cluster distance (see Table 1). There is excellent agreement between our values and those obtained from spectra, as expected for a cluster with an isotropic velocity distribution and a correctly estimated distance. This once again confirms the high quality and reliability of our PM catalog.

Here and henceforth, velocity dispersions were estimated from the PM catalog using the same method as in van der Marel & Anderson (2010). This corrects the observed scatter for the individual stellar PM uncertainties. Unless stated otherwise, we quote the average one-dimensional velocity dispersion σ_μ, based on the combined x and y PM measurements. Moreover, we adopted an appropriate sample of high-quality PM stars for the analysis.

Satisfied that our PM measurements appear to be solid both internally (see Section 6) and externally (see Section 8.2), we proceed by analyzing more in detail the MS velocity–dispersion profile of NGC 7078. In order to select the best-measured stars, we proceeded as follows. First, we selected likely cluster members on the basis of their positions on the CMD. In addition, we kept only those stars with QFIT-percentile values below 50%, reduced χ^2 values below 1.25, and $N_R > 0.85$ that proved to remove crowding or blending as a source of systematic effects (see Section 7.5).

Then we adopted an iterative procedure that further identifies and rejects stars for which the measurement error is larger than F times the local σ_μ, where F is a certain threshold value, and the local σ_μ is computed for each star using the 100 stars closest in radial distance and magnitude to the target star. We iterated this procedure until we obtained convergence of the dispersion profiles. We found that F = 0.5 provides the best compromise between accuracy and sample size. After these procedures were applied, there were no remaining candidate field stars with highly discrepant ($>5\sigma$) PMs. Our final sample consists of 18 136 stars, of which 15 456 are MS stars with $m_{\rm F606W}$ magnitudes between 19.15 (which here defines the turnoff) and 22.7, and between 11″.6 and 136″.6 from the cluster center.

We divided this sample into 8 mag bins each having approximately the same number of stars, and into 10 radial intervals, again each having approximately the same number of stars. These subdivisions define 80 regions in the magnitude–radius space, with each containing on average 193 stars. Obviously, the innermost radial intervals have fewer faint stars on average than the outermost ones because of crowding-driven incompleteness. The number of stars in each region ranges from 72 to 342. For each region we computed the velocity dispersion σ_μ and its error for both amplifier-based and locally corrected PMs.

Figure 21 collects the results of the velocity–dispersion analysis. We show the results in two ways: (1) σ_μ as a function of the magnitude for different radial intervals (top panels) and (2) σ_μ as a function of the radial distance for different magnitude bins (bottom panels). Panels (a) and (e) show the CMD of selected stars around the MS of NGC 7078. Horizontal lines delimit the magnitude bins. Panels (b) and (f) show the spatial distribution of the selected stars. The circles define the radial intervals. Panels (c) and (d) show the σ_μ profiles as a function of the $m_{\rm F606W}$ magnitude for locally corrected and amplifier-based PMs, respectively. Points and error bars are color-coded according to their radial intervals. Panels (g) and (h) show the σ_μ profiles as a function of the radial distance from the cluster center, with points and error bars color-coded according to their magnitude bin.

Figure 21 reveals a complex behavior of σ_μ as a function of both magnitude and radius. Bright, more massive stars are kinematically colder than faint, less massive stars at all radii. This behavior is a direct consequence of the effects of energy equipartition. Moreover, stars at larger radii are colder than stars closer to the cluster center for each magnitude bin, which is a direct consequence of hydrostatic equilibrium. There is little (a statistically insignificant) difference between amplifier-based and locally corrected velocity–dispersion profiles, with the latter being on average only slightly lower than the former. Figure 21

[21] Gerssen et al. (2002) published individual star velocities and unparameterized profiles of V and σ_V of stars in the core of the NGC 7078, obtained with the *HST* STIS spectrograph; den Brok et al. (2014) combined Gerssen et al. (2002) velocities with those of Gebhardt et al. (2000) to compute radial-binned profiles. Here we consider only the innermost three data points of the den Brok et al. (2014) profile (their Figure 1), which are mostly (if not completely) derived using the Gerssen et al. (2002) data.

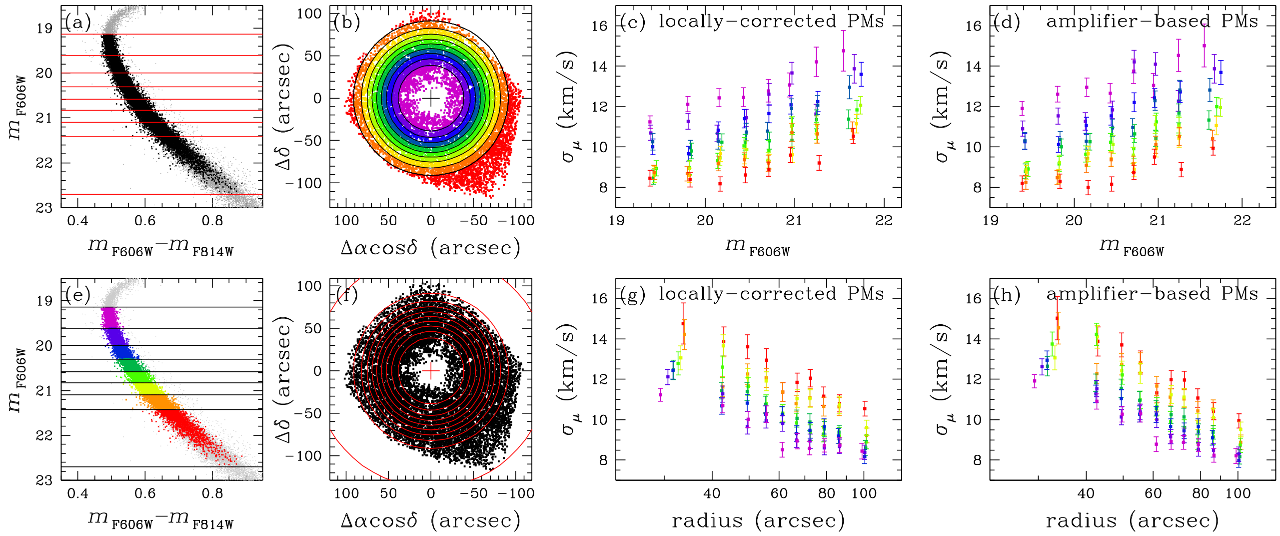

Figure 21. Top panels show the velocity–dispersion profiles σ_μ of MS stars in different radial intervals as a function of the $m_{\rm F606W}$ magnitude. (a) The CMD of NGC 7078 around its MS for all selected stars (gray) and for those with PM errors smaller than half the local velocity dispersion (black). The red lines define 8 mag bins with the same number of stars. (b) The spatial distribution of high-quality-PM MS stars. The black circles define 10 radial intervals with the same number of stars. Panels (c) and (d) show σ_μ values as a function of $m_{\rm F606W}$ for the locally corrected and amplifier-based PMs, respectively. Points and error bars are color-coded according to their radial interval. Bottom panels show the σ_μ profiles for the same stars in different magnitude intervals as a function of their distance from the cluster center. The magnitude and radial bins are the same as in the top panels. These time points are color-coded according to their magnitude bin.

(A color version of this figure is available in the online journal.)

also tells us that the LOS velocity dispersions quoted in the literature based on RGB stars are to be considered as lower limits. The vast majority of stars are less massive than RGB stars and move faster.

8.4. Anisotropy

A direct estimate of the degree of velocity anisotropy of the cluster is obtained by studying the ratio between tangential and radial proper motion dispersions as a function of the radial distance. We measured the velocity dispersion in each direction, using the full sample of 15,546 high-quality stars, in order to map the velocity–anisotropy profile. Moreover, velocity dispersions are computed using both amplifier-based and locally corrected PM values.

The results are summarized in Figure 22, using amplifier-based PMs in the top panel and locally corrected PMs in the bottom panel. As before, there is only a small difference between the two ways of computing PMs. The velocity distribution of NGC 7078 in the central ∼45″ (comparable to the half-light radius $r_{\rm h} = 60''$; Harris 1996, 2010 edition) is close to isotropic. This is consistent with what might be expected given the short two-body relaxation time of NGC 7078. There is evidence of motions that are preferably oriented radially rather than tangentially at distances greater than 45″.

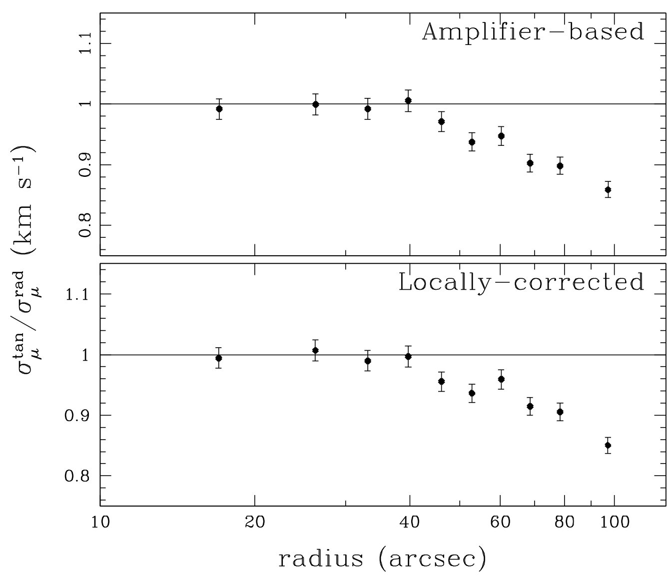

Figure 22. Anisotropy in the proper motion velocity dispersion as a function of the radial distance. Amplifier-based PMs are in the top panel, and locally corrected PMs are in the bottom one.

9. CONCLUSIONS AND DISCUSSION

Our understanding of the internal kinematics of GCs is based largely on studies of modest samples of stellar LOS velocities. PM studies with the *HST* have the potential to significantly advance our understanding, by extending the measurements to two- or three-dimensional velocities, lower stellar masses, and larger sample sizes. We have presented here the first study of *HST* PMs for a large sample of GCs, based on heterogenous data assembled from the *HST* archive. This first paper in a series has focused on the data reduction procedures, data quality, and new kinematic quantities inferred for NGC 7078 (M 15). Subsequent papers will explore a range of applications, including the many scientific topics of interest highlighted in Section 1.

We identified clusters in the *HST* archive with suitable exposures spread over multiple epochs, resulting in a sample of 22 clusters. For these clusters we analyzed a total of 2510 different exposures, obtained over the past decade with the ACS/WFC, ACS/HRC, and WFC3/UVIS instruments. We created photometric, astrometric, and PM catalogs from these data. For this, we used and extended the software developed in the context of our previous GC studies and in the context of our HSTPROMO collaboration. The data reduction also folded in and improved many of the single-epoch catalogs previously obtained in the context of the *HST* Globular Cluster Treasury

Table 7
List of Observations of NGC 104

GO	PI	Intr./Cam.	Filter	$N\times$Exp. Time	Epoch
9019	Bohlin	ACS/HRC	F330W	18 × 66s	2002 Apr
			F435W	2 × 5s, 2 × 20s, 17 × 60s, 2×300s	
			F475W	10 × 60s	
			F555W	14 × 60s	
			F606W	10 × 60s	
			F625W	10 × 60s	
			F775W	13 × 60s	
			F814W	2 × 5s, 2 × 20s, 14 × 60s, 2 × 300s	
			F850LP	10 × 60s	
9028	Meurer	ACS/HRC	F475W	40 × 60s	2002 Apr
		ACS/WFC	F475W	20 × 60s	
9281	Grindlay	ACS/WFC	F435W	1 × 10s, 6 × 100s, 3 × 115	2002 Sep-Oct
			F625W	2 × 10s, 20 × 65s	
			F658N	6 × 350s, 6 × 370s, 8 × 390s	
9575	Sparks	ACS/WFC	F475W	3 × 700s	2002 Apr
			F775W	1 × 578s, 5 × 700s	
			F850LP	6 × 700s	
9443	King	ACS/HRC	F330W	1 × 350s	2002 Jul
			F435W	1 × 350s	
			F475W	20 × 60s, 1 × 350s	
			F555W	1 × 350s	
			F606W	1 × 350s	
			F814W	1 × 350s	
		ACS/WFC	F435W	1 × 150s	
			F475W	5 × 60s, 1 × 150s	
			F555W	1 × 150s	
			F606W	1 × 100s	
			F814W	1 × 150s	
9453	Brown	ACS/WFC	F606W	1 × 6s, 1 × 70s	2002 Jul
			F814W	1 × 5s, 1 × 72s	
9662	Gilliland	ACS/HRC	F606W	2 × 1s	2002 Sep
9503	Nagar	ACS/WFC	F475W	1 × 60s	2003 Jan
			F658N	1 × 340s	
10055	Biretta	ACS/HRC	F330W	2 × 40s, 6 × 150s	2004 Feb
			F435W	2 × 20s, 6 × 60s	
			F606W	2 × 10s	
			F775W	2 × 10s	
10375	Mack	ACS/HRC	F435W	4 × 60s	2004–2005
			F475W	4 × 60s	
			F555W	4 × 60s	
			F606W	4 × 60s	
			F625W	4 × 60s	
			F775W	4 × 60s	
			F814W	4 × 60s	
			F850LP	4 × 60s	
10737	Mack	ACS/HRC	F330W	2 × 66s	2005–2006
			F435W	6 × 60s	
			F475W	6 × 60s	
			F555W	6 × 60s	
			F606W	6 × 60s	
			F625W	6 × 60s	
			F775W	6 × 60s	
			F814W	6 × 60s	
			F850LP	6 × 60s	
10775	Sarajedini	ACS/WFC	F606W	1 × 3s, 4 × 50s	2006 Mar
			F814W	1 × 3s, 4 × 50s	
11664	Brown	WFC3/UVIS	F390W	2 × 10s, 2 × 348s, 2 × 940s	2010 Sep
			F555W	1 × 1s, 1 × 30s, 2 × 665s	
			F814W	1 × 30s, 2 × 565s	
11729	Holtzman	WFC3/UVIS	F336W	1 × 30s, 2 × 580s	2010 Sep
			F390W	1 × 10s	
			F467M	1 × 40s, 2 × 450s	
12116	Dalcanton	ACS/WFC	F475W	2 × 7s	2012 Jul

Table 8
List of Observations of NGC 288

GO	PI	Intr./Cam.	Filter	$N\times$Exp. Time	Epoch
10120	Anderson	ACS/WFC	F435W	1 × 60s, 2 × 340s	2004 Sep
			F625W	1 × 10s, 1 × 75s, 1 × 115s, 1 × 120s	
			F658N	2 × 340, 2 × 540x	
10775	Sarajedini	ACS/WFC	F606W	2 × 10s, 8 × 130s	2006 Jul
			F814W	2 × 10s, 8 × 150s	
12193	Lee	WFC3/UVIS	F467M	1 × 964s, 1 × 1055s	2010 Nov

Table 9
List of Observations of NGC 362

GO	PI	Intr./Cam.	Filter	$N\times$Exp. Time	Epoch
10005	Lewin	ACS/WFC	F435W	4 × 340s	2003 Dec
			F625W	2 × 110s, 2 × 120s	
			F658N	2 × 440s, 2 × 500s	
10401	Chandar	ACS/HRC	F435W	17 × 85s	2004 Dec
10615	Anderson	ACS/WFC	F435W	5 × 70s, 30 × 340s	2005 Sep
10775	Sarajedini	ACS/WFC	F606W	1 × 10s, 4 × 150s	2006 Jun
			F814W	1 × 10s, 4 × 170s	

Table 10
List of Observations of NGC 1851

GO	PI	Intr./Cam.	Filter	$N\times$Exp. Time	Epoch
10458	Biretta	ACS/HRC	F555W	12 × 10s, 4 × 100s, 2 × 500s	2005 Aug
10775	Sarajedini	ACS/WFC	F606W	1 × 20s, 5 × 350s	2006 May
			F814W	1 × 20s, 5 × 350s	
12311	Piotto	WFC3/UVIS	F814W	7 × 100s	2010–2011

Table 11
List of Observations of NGC 2808

GO	PI	Intr./Cam.	Filter	$N\times$Exp. Time	Epoch
9899	Piotto	ACS/WFC	F475W	6 × 340s	2004 May
10335	Ford	ACS/HRC	F435W	24 × 135s	2006 Jun
			F555W	4 × 50s	
10775	Sarajedini	ACS/WFC	F606W	1 × 23s, 4 × 360s	2006 Mar
			F814W	1 × 23s, 4 × 370s	
10922	Piotto	ACS/WFC	F475W	1 × 20s, 2 × 350s, 2 × 360s	2006 Aug–Nov
			F814W	1 × 10s, 3 × 350s, 4 × 360s	
11801	Ford	WFC3/UVIS	F438W	7 × 20s, 9 × 160s	2009 Dec

Program GO-10775. Significant effort was invested to develop a reduction procedure that can be used in a homogeneous way for all clusters to obtain high-quality PM measurements, despite the very heterogeneous nature of the archival data (which were not generally obtained for high-precision astrometry).

We demonstrated the quality of the PM measurements through extensive Monte Carlo simulations for single stars and comprehensive data sets. These show that input PM distributions and dispersions can be reliably recovered for realistic observational setups and random errors. In practice, we also have to contend with various sources of systematic errors. We have discussed in detail the effects on the PM measurements that are due to charge-transfer-inefficiency effects, uncorrected geometric-distortion residuals, and crowding and blending. We have developed and discussed techniques to remove systematic PM errors that are due to these effects to the extent possible.

Table 12
List of Observations of NGC 5139

GO	PI	Intr./Cam.	Filter	$N \times$Exp. Time	Epoch
9442	Cool	ACS/WFC	F435W	9 × 12s, 27 × 340s	2002 Jun
			F625W	8 × 8s, 27 × 340s	
			F658N	36 × 440s	
10252	Anderson	ACS/WFC	F606W	1 × 15s, 5 × 340s	2004 Dec
			F814W	1 × 15s, 5 × 340s	
10775	Sarajedini	ACS/WFC	F606W	1 × 4s, 4 × 80s	2006 Mar–Jul
			F814W	1 × 4s, 4 × 80s	
11452	Kim Quijano	WFC3/UVIS	F336W	9 × 350s	2009 Jul
			F606W	1 × 35s	
			F814W	1 × 35s	
11911	Sabbi	WFC3/UVIS	F336W	19 × 350s	2010 Jan–Jul
			F390W	15 × 350s	
			F438W	25 × 350s	
			F555W	18 × 40s	
			F606W	22 × 40s	
			F775W	16 × 350s	
			F814W	24 × 40s	
			F850LP	17 × 60s	
12094	Petro	WFC3/UVIS	F606W	9 × 40s	2010 Apr
12339	Sabbi	WFC3/UVIS	F336W	9 × 350s	2011 Feb–Mar
			F438W	9 × 350s	
			F555W	9 × 40s	
			F606W	9 × 40s	
			F814W	9 × 40s	
			F850LP	9 × 60s	
12353	Kozhurina-Platais	WFC3/UVIS	F606W	11 × 40s	2010–2011
12694	Long	WFC3/UVIS	F467M	3 × 400s, 3 × 450s	2012 Feb–Apr
12700	Riess	WFC3/UVIS	F775W	2 × 450s	2012 Jun
12714	Kozhurina-Platais	WFC3/UVIS	F606W	4 × 40s	2012 Mar
13100	Kozhurina-Platais	WFC3/UVIS	F606W	6 × 48s	2012–2013

Table 13
List of Observations of NGC 5904

GO	PI	Intr./Cam.	Filter	$N \times$Exp. Time	Epoch
10120	Anderson	ACS/WFC	F435W	1 × 70s, 2 × 340s	2004 Aug
			F625W	1 × 10s, 1 × 70s, 2 × 110s	
			F658N	2 × 340s, 2 × 540s	
10615	Anderson	ACS/WFC	F435W	1 × 130s, 3 × 215s, 25 × 240s	2006 Feb
10775	Sarajedini	ACS/WFC	F606W	1 × 7s, 4 × 140s	2006 Mar
			F814W	1 × 7s, 4 × 140s	
11615	Ferraro	WFC3/UVIS	F390W	6 × 500s	2010 Jul
			F606W	4 × 150s	
			F814W	4 × 150s	

We have presented various tests that have shown that with these corrections, our PM data quality is excellent.

From our analyses we were able to measure the PM of over 1.3 million stars in the central regions of the target clusters, with a median number of ∼60,000 stars per cluster. Most of the PM catalogs will be disseminated as parts of future papers in this series. Here we focus on, and release, the catalog for NGC 7078, which consists of 77,837 stars. The number of stars with measured velocities is ∼40 times larger than in the best catalogs of NGC 7078 PMs and LOS velocities previously available (Gebhardt et al. 2000; McNamara et al. 2004). Our measurements are consistent with these previous catalogs in the areas of overlap. For the PMs, we demonstrated this on a star-by-star basis, and for the LOS velocities, we demonstrated this by comparison of the velocity–dispersion profiles for bright stars under the assumption of isotropy.

Table 14
List of Observations of NGC 5927

GO	PI	Intr./Cam.	Filter	$N \times$Exp. Time	Epoch
9453	Brown	ACS/WFC	F606W	1 × 2s, 1 × 30s, 1 × 500s	2002 Aug
			F814W	1 × 15s, 1 × 340s	
10775	Sarajedini	ACS/WFC	F606W	1 × 30s, 5 × 350s	2006 Apr
			F814W	1 × 25s, 5 × 360s	
11664	Brown	WFC3/UVIS	F390W	2 × 40s, 2 × 348s, 2 × 800s	2010 Aug
			F555W	1 × 50s, 2 × 665s	
			F814W	1 × 50s, 2 × 455s	
11729	Holtzman	WFC3/UVIS	F336W	2 × 475s	2010 Sep
			F467M	2 × 365s	

Table 15
List of Observations of NGC 6266

GO	PI	Intr./Cam.	Filter	$N \times$Exp. Time	Epoch
10120	Anderson	ACS/WFC	F435W	1 × 200s, 2 × 340s	2004 Aug
			F625W	1 × 30s, 1 × 120s, 3 × 340s	
			F658N	1 × 340s, 3 × 350s, 3 × 365s, 3 × 375s	
11609	Chanamé	WFC3/UVIS	F390W	4 × 35s, 5 × 393s, 5 × 421s	2010 Jun

Table 16
List of Observations of NGC 6341

GO	PI	Intr./Cam.	Filter	$N \times$Exp. Time	Epoch
9453	Brown	ACS/WFC	F606W	1 × 5s, 1 × 90s	2002 Aug
			F814W	1 × 6s, 1 × 100s	
10120	Anderson	ACS/WFC	F435W	1 × 90s, 2 × 340s	2004 Aug
			F625W	1 × 10s, 3 × 120s	
			F658N	2 × 350s, 2 × 555s	
10335	Ford	ACS/HRC	F435W	36 × 85s	2004–2006
			F435W	15 × 40s	
10443	Biretta	ACS/HRC	F330W	8 × 100s, 4 × 500s	2005 Feb
			F555W	78 × 10s, 33 × 100s, 18 × 500s	
			F606W	14 × 357	
10455	Biretta	ACS/HRC	F555W	12 × 10s, 41 × 100s, 2 × 500s	2005 Feb
10505	Gallart	ACS/WFC	F475W	1 × 3s, 1 × 20s, 1 × 40s	2006 Jan
			F814W	1 × 7s, 1 × 10s, 1 × 20s	
10615	Anderson	ACS/WFC	F435W	30 × 340s	2006 Jan
10775	Sarajedini	ACS/WFC	F606W	1 × 7s, 5 × 140s	2006 Apr
			F814W	1 × 7s, 5 × 150s	
11664	Brown	WFC3/UVIS	F390W	2 × 348s, 2 × 795s	2009 Oct
			F555W	1 × 30s, 2 × 665s	
			F814W	1 × 30s, 2 × 415s	
11801	Ford	WFC3/UVIS	F438W	6 × 10s, 11 × 110s	2009 Nov
11729	Holtzman	WFC3/UVIS	F336W	1 × 30s, 2 × 425s	2010 Oct
			F390W	1 × 10s	
			F467M	1 × 40s, 2 × 350s	

Table 17
List of Observations of NGC 6362

GO	PI	Intr./Cam.	Filter	$N \times$Exp. Time	Epoch
10775	Sarajedini	ACS/WFC	F606W	1 × 10s, 4 × 130s	2006 May
			F814W	1 × 10s, 4 × 150s	
12008	Kong	WFC3/UVIS	F336W	1 × 368s, 5 × 450s	2010 Aug

Table 18
List of Observations of NGC 6388

GO	PI	Intr./Cam.	Filter	$N \times$Exp. Time	Epoch
9821	Pritzl	ACS/WFC	F435W	6 × 11s	2003–2004
			F555W	6 × 7s	
			F814W	6 × 3s	
9835	Drukier	ACS/HRC	F555W	48 × 155s	2003 Oct
			F814W	5 × 25s, 2 × 469s, 10 × 505s	
10350	Cohn	ACS/HRC	F330W	2 × 1266s, 4 × 1314s	2006 Apr
			F555W	3 × 155s	
10474	Drukier	ACS/HRC	F555W	48 × 155s	2006 Apr
			F814W	4 × 25s, 8 × 501s, 4 × 508s	
10775	Sarajedini	ACS/WFC	F606W	1 × 40s, 5 × 340s	2006 Apr
			F814W	1 × 40s, 5 × 350s	
11739	Piotto	WFC3/UVIS	F390W	6 × 880s	2010 Jun–Jul

Table 19
List of Observations of NGC 6397

GO	PI	Intr./Cam.	Filter	$N \times$Exp. Time	Epoch
10257	Anderson	ACS/WFC	F435W	5 × 13s, 5 × 340s	2004–2005
			F625W	5 × 10s, 5 × 340s	
			F658N	20 × 390s, 20 × 395s	
10775	Sarajedini	ACS/WFC	F606W	1 × 1s, 4 × 15s	2006 May
			F814W	1 × 1s, 4 × 15s	
11633	Rich	WFC3/UVIS	F336W	6 × 620s	2010 Mar
			F606W	6 × 360s	

Table 20
List of Observations of NGC 6441

GO	PI	Intr./Cam.	Filter	$N \times$Exp. Time	Epoch
9835	Drukier	ACS/HRC	F555W	36 × 240s	2003 Sep
			F814W	5 × 40s, 2 × 413s, 10 × 440s	
10775	Sarajedini	ACS/WFC	F606W	1 × 45s, 5 × 340s	2006 May
			F814W	1 × 45s, 5 × 350s	
11739	Piotto	WFC3/UVIS	F390W	2 × 880s, 2 × 884s, 8 × 885s	2010–2011

Table 21
List of Observations of NGC 6535

GO	PI	Intr./Cam.	Filter	$N \times$Exp. Time	Epoch
10775	Sarajedini	ACS/WFC	F606W	1 × 12s, 4 × 130s	2006 Mar
			F814W	1 × 12s, 4 × 150s	
12008	Kong	ACS/WFC	F625W	1 × 100s, 1 × 148s	2010 Sep
			F658N	1 × 588s, 1 × 600s	
		WFC3/UVIS	F336W	1 × 253s, 5 × 400s	

Table 22
List of Observations of NGC 6624

GO	PI	Intr./Cam.	Filter	$N \times$Exp. Time	Epoch
10401	Chandar	ACS/HRC	F435W	20 × 200s	2005 Feb
10775	Sarajedini	ACS/WFC	F606W	1 × 15s, 5 × 350s	2006 Apr
			F814W	1 × 15s, 5 × 350s	
10573	Mateo	ACS/WFC	F435W	1 × 360s	2006 Jun
			F555W	1 × 160s	
			F814W	1 × 65s	

We present a preliminary analysis of the PM kinematics of NGC 7078 that demonstrates the potential of our data. The large number of measurements allows detailed studies of the velocity dispersion as a function of radius, as a function of stellar magnitude (or mass) along the main sequence, and as a function of direction in the plane of the sky (radial or tangential). The velocity dispersion increases toward the center as expected from hydrostatic equilibrium, and it increases toward lower masses as expected from energy equipartition. The velocity dispersion is isotropic near the center, as expected from two-body relaxation. There is evidence of motions that are preferably oriented radially rather than tangentially outside the half-light radius.

Although this work represents the most detailed study of GC PMs to date, there continues to be room for significant

Table 23
List of Observations of NGC 6656

GO	PI	Intr./Cam.	Filter	$N \times$Exp. Time	Epoch
10775	Sarajedini	ACS/WFC	F606W	1 × 3s, 4 × 55s	2006 Apr
			F814W	1 × 3s, 4 × 65s	
11558	De Marco	ACS/WFC	F502N	2 × 441s, 1 × 2102x, 1 × 2322s	2010 Mar
12311	Piotto	WFC3/UVIS	F814W	4 × 50s	2010–2011

Table 24
List of Observations of NGC 6681

GO	PI	Intr./Cam.	Filter	$N \times$Exp. Time	Epoch
9019	Bohlin	ACS/HRC	F330W	4 × 170s	2002 Apr
9010	Tran	ACS/HRC	F330W	6 × 70s	2002 May–June
9565	De Marchi	ACS/HRC	F330W	16 × 70s	2002 Jun-Sep
9566	De Marchi	ACS/HRC	F330W	17 × 70s	2003 Feb
9655	Giavalisco	ACS/HRC	F330W	16 × 70s	2003 Feb–Sep
10047	Giavalisco	ACS/HRC	F330W	6 × 70s	2004 Mar–Sep
10401	Chandar	ACS/HRC	F435W	26 × 125s	2005 Feb
10373	Giavalisco	ACS/HRC	F330W	4 × 70s	2005–2006
10736	Maiz-Apellaniz	ACS/HRC	F330W	8 × 20s	2006 Mar
			F435W	4 × 2s	
			F555W	4 × 2s	
			F625W	4 × 1s	
			F814W	4 × 1s	
10775	Sarajedini	ACS/WFC	F606W	1 × 10s, 4 × 140s	2006 May
			F814W	1 × 10s, 4 × 150s	
12516	Ferraro	WFC3/UVIS	F390W	12 × 348s	2011 Nov
			F555W	2 × 127s, 8 × 150s	
			F814W	13 × 348s	

Table 25
List of Observations of NGC 6752

GO	PI	Intr./Cam.	Filter	$N \times$Exp. Time	Epoch
9453	Brown	ACS/WFC	F606W	1 × 4s, 1 × 40s	2002 Sep
			F814W	1 × 4s, 1 × 45s	
9899	Piotto	ACS/WFC	F475W	6 × 340s	2004 Jul
10121	Bailyn	ACS/WFC	F555W	12 × 80s, 11 × 435s	2004 Sep
			F814W	12 × 40s	
10335	Ford	ACS/HRC	F435W	24 × 35s	2004–2006
			F555W	13 × 10s	
10458	Biretta	ACS/HRC	F555W	12 × 10s, 4 × 100s, 2 × 500s	2005 Aug
			F606W	2 × 357s	
10459	Biretta	ACS/WFC	F606W	8 × 450	2005 Oct
10335	Ford	ACS/HRC	F435W	24 × 35s	2004 Jun
			F555W	13 × 10s	
10775	Sarajedini	ACS/WFC	F606W	1 × 2s, 4 × 35s	2006 May
			F814W	1 × 2s, 4 × 40s	
11801	Ford	WFC3/UVIS	F438W	4 × 5s, 18 × 45s	2009 Nov
11664	Brown	WFC3/UVIS	F390W	2 × 348s, 2 × 880s	2010 May
			F555W	1 × 30s, 2 × 665s	
			F814W	1 × 30s, 2 × 495s	
11904	Kalirai	WFC3/UVIS	F555W	15 × 550s	2010 Jul–Aug
			F814W	15 × 550s	
12254	Cool	ACS/WFC	F435W	6 × 10s, 12 × 380s	2011 May–Nov
			F625W	18 × 10s, 12 × 360s	
			F658N	12 × 724s, 12 × 820s	
12311	Piotto	WFC3/UVIS	F814W	2 × 50s	2011 Mar–Apr

Table 26
List of Observations of NGC 6715

GO	PI	Intr./Cam.	Filter	$N \times$Exp. Time	Epoch
10775	Sarajedini	ACS/WFC	F606W	2 × 30s, 10 × 340s	2006 May
			F814W	2 × 30s, 10 × 350s	
12274	van der Marel	WFC3/UVIS	F438W	10 × 30s, 5 × 234s, 5 × 256s	2011 Sep

Table 27
List of Observations of NGC 7078

GO	PI	Intr./Cam.	Filter	$N \times$Exp. Time	Epoch
10401	Chandar	ACS/HRC	F435W	13 × 125s	2004 Dec
10775	Sarajedini	ACS/WFC	F606W	1 × 15s, 4 × 130s	2006 May
			F814W	1 × 15s, 4 × 150s	
11233	Piotto	WFC3/UVIS	F390W	6 × 827s	2010 May
12605	Piotto	WFC3/UVIS	F336W	6 × 350s	2011 Oct
			F438W	6 × 65s	

Table 28
List of Observations of NGC 7099

GO	PI	Intr./Cam.	Filter	$N \times$Exp. Time	Epoch
10401	Chandar	ACS/HRC	F435W	13 × 125s	2004 Dec
10775	Sarajedini	ACS/WFC	F606W	1 × 7s, 4 × 140s	2006 May
			F814W	1 × 7s, 4 × 140s	

improvement in the observations and measurements. New observations of the cores of GCs are taken in each *HST* observing cycle. This makes it possible to construct PM catalogs for more clusters and to extend the time baselines (and reduce the uncertainties) for clusters with existing PM catalogs. Also, the measurements presented here were not optimized to deal with very crowded fields. Some clusters have deep ACS/HRC observations of their cores. These have higher spatial resolution than the ACS/WFC observations that were used to build the GO-10775 master frames used for our analysis. Moreover, these ACS/HRC observations are often taken in bluer filters, which will yield less crowding (because the brightest stars tend to be *red* giants). New photometric reduction techniques for the WFC3 detector (J. Anderson et al., in preparation) can measure stellar positions and fluxes after subtraction of surrounding neighbors (deblending; see Anderson et al. 2008 for ACS/WFC). Master frames based on the ACS/HRC observations, combined with data reduction techniques that explicitly deblend, have the potential to yield catalogs with more stars with more accurately measured PMs and better characterized errors. This is especially relevant close to the cluster centers, which are dominated by crowding and blending issues. These central regions are crucial for studies of intermediate-mass black holes in GCs.

We thank the anonymous referee for comments that helped improve the presentation of our results. Support for this work was provided by grants for *HST* programs GO-9453, GO-10335, GO-10401, GO-11664, GO-11801, GO-12274, AR-12656, and AR-12845, provided by the Space Telescope Science Institute, which is operated by AURA, Inc., under NASA contract NAS 5-26555. F.R.F. and D.M. acknowledge the support from the Cosmic-Lab project (Web site: http://www.cosmic-lab.eu) funded by the European Research Council (under contract ERC-2010-AdG-267675). P.B. acknowledges financial support from the International Max Planck Research School for Astronomy and Cosmic Physics (IMPRS) at the University of Heidelberg and travel support from the Heidelberg Graduate School for Fundamental Physics (HGSFP). The authors are grateful to Laura Ferrarese, Rodrigo Ibata, and Carlton Pryor for help with the proposal preparation for some of these projects and to Michele Trenti for helpful discussions.

APPENDIX A

COMPLETE LIST OF THE DATA SETS USED FOR EACH CLUSTER

Tables 7–28 provide the full list of used exposures for each cluster, ordered by program number, camera, and filter. These tables are available only in the electronic version of the article.

APPENDIX B

PROPER-MOTION CATALOG OF NGC 7078

Our procedures generate a large number of parameters for each star, but most users will need only the high-level data. The PM catalog of NGC 7078 contains 91 lines of header information, followed by one line for each star with a PM measurement, for a total of 77,837 stars. Stars in the catalog are sorted according to their distance from the cluster center, as given in Table 1.

The header starts with some general information about the cluster, such as the reference time of the master frame and the adopted cluster center position, in both equatorial and master-frame units. Then follows a column-by-column description of the catalog. The columns contain the reference-frame positions and distance from the cluster center, calibrated and differential-reddening-corrected F606W and F814W magnitudes with errors and some photometric-quality information, PMs with errors derived using both the expected errors as a weight and the actual residuals around the PM least-squares fits (see Section 6.1), some additional astrometric-quality information, and finally the differences between local-corrected and amplifier-based PMs (see Section 7.4). A description of each column of the catalog is given in Table 29, and the first 10 lines of the NGC 7078 PM catalog are shown in Table 30.

Table 29
Column-by-column Information Contained in the Catalog

Col	Name (unit)	Explanation
		Astrometric information
1	r ($''$)	Distance from the cluster center
2	Δx_0 ($''$)	GO-10775 x-position in the rectified Cartesian system with respect to the adopted center
3	Δy_0 ($''$)	GO-10775 y-position in the rectified Cartesian system with respect to the adopted center
4	$\mu_\alpha \cos\delta$ (mas yr^{-1})	PM along the x-axis (parallel to and increasing as R.A.)
5	μ_δ (mas yr^{-1})	PM along the y-axis (parallel to and increasing as Dec.)
6	$\sigma_{\mu_\alpha \cos\delta}$ (mas yr^{-1})	1σ uncertainty in $\mu_\alpha \cos\delta$ computed using actual residuals
7	σ_{μ_δ} (mas yr^{-1})	1σ uncertainty in μ_δ computed using actual residuals
8	$x_{\rm M}$ (pixel)	x-position on the master frame
9	$y_{\rm M}$ (pixel)	y-position on the master frame
10	Δx (pixel)	Difference between $x_{\rm M}$ and the PM-predicted position at the reference time ($\overline{x}$)
11	Δy (pixel)	Difference between $y_{\rm M}$ and the PM-predicted position at the reference time ($\overline{y}$)
12	err$_{\mu_\alpha \cos\delta}$ (mas yr^{-1})	1σ uncertainty in $\mu_\alpha \cos\delta$ computed using expected errors
13	err$_{\mu_\delta}$ (mas yr^{-1})	1σ uncertainty in μ_δ computed using expected errors
		Photometric information
14	$m_{\rm F606W}$ (mag)	Differential-reddening-corrected GO-10775 F606W Vega-mag photometry
15	$m_{\rm F814W}$ (mag)	Differential-reddening-corrected GO-10775 F814W Vega-mag photometry
16	$\sigma_{m_{\rm F606W}}$ (mag)	Photometric error in F606W (from GO-10775)
17	$\sigma_{m_{\rm F814W}}$ (mag)	Photometric error in F814W (from GO-10775)
18	$\texttt{QFIT}_{\rm F606W}$	Quality of F606W PSF-fit (from GO-10775)
19	$\texttt{QFIT}_{\rm F814W}$	Quality of F814W PSF-fit (from GO-10775)
		Proper-motion quality information
20	$\chi^2_{\mu_\alpha \cos\delta}$	Reduced χ^2 of the fit of the x-component of the motion
21	$\chi^2_{\mu_\delta}$	Reduced χ^2 of the fit of the y-component of the motion
22	$\sigma_{\overline{x}}$ (pix)	1σ uncertainty in the intercept of the PM fit for the x-component using actual residuals
23	$\sigma_{\overline{y}}$ (pix)	1σ uncertainty in the intercept of the PM fit for the y-component using actual residuals
24	time (yr)	Time baseline, in Julian years
25	err$_{\overline{x}}$ (pix)	1σ uncertainty in the intercept of the PM fit for the x-component using expected errors
26	err$_{\overline{y}}$ (pix)	1σ uncertainty in the intercept of the PM fit for the y-component using expected errors
27	U$_{\rm ref}$	Flag: 1 if used as reference bona fide cluster star for the linear transformations, 0 otherwise
28	N$_{\rm found}$	Initial number of data points for the PM fits
29	N$_{\rm used}$	Final number of data points used for the PM fits
30	ID	ID number for each star (not the GO-10775 ID)
		Local PM corrections
31	$\Delta\mu_\alpha \cos\delta$ (mas yr^{-1})	Difference in $\mu_\alpha \cos\delta$ between locally corrected and amplifier-based PMs. Add to column 4 to obtain locally corrected PMs.
32	$\Delta\mu_\delta$ (mas yr^{-1})	Difference in μ_δ between locally corrected and amplifier-based PMs. Add to column 5 to obtain locally corrected PMs.

Table 30
First 10 Lines of the NGC 7078 PM Catalog

r ($''$) (1)	Δx_0 ($''$) (2)	Δy_0 ($''$) (3)	$\mu_\alpha \cos\delta$ (4)	μ_δ (5)	$\sigma_{\mu_\alpha \cos\delta}$ (6)	σ_{μ_δ} (7)	$x_{\rm M}$ (8)	$y_{\rm M}$ (9)	Δx (10)	Δy (11)	${\rm err}_{\mu_\alpha \cos\delta}$ (12)	${\rm err}_{\mu_\delta}$ (13)	$m_{\rm F606W}$ (14)	$m_{\rm F814W}$ (15)	$\sigma_{m_{\rm F606W}}$ (16)	→
0.22148	0.19883	0.09756	−0.203	0.249	0.039	0.030	4984.312	5019.940	0.024	0.014	0.032	0.030	17.015	16.276	9.900	...
0.50339	0.24141	0.44172	−3.057	9.266	0.367	2.021	4983.246	5028.540	−0.078	−0.241	0.418	0.957	18.253	17.774	9.900	...
1.13357	0.84530	0.75528	0.201	0.245	0.045	0.054	4968.149	5036.379	0.030	0.003	0.042	0.037	15.508	15.113	9.900	...
1.24526	1.18454	0.38412	−0.283	0.055	0.020	0.038	4959.674	5027.097	−0.014	0.052	0.021	0.034	15.985	15.801	9.900	...
1.32849	0.86993	1.00404	0.001	−0.192	0.023	0.021	4967.535	5042.601	0.012	−0.008	0.024	0.018	16.974	16.193	9.900	...
1.33293	0.59227	1.19412	0.321	−0.101	0.027	0.031	4974.479	5047.344	0.004	−0.013	0.027	0.035	17.419	16.724	9.900	...
1.46104	−1.44918	0.18576	0.176	−0.084	0.022	0.023	5025.506	5022.140	0.016	0.012	0.018	0.028	16.686	15.977	9.900	...
1.62112	−0.24352	1.60272	0.054	−0.045	0.034	0.019	4995.371	5057.557	−0.030	0.022	0.029	0.023	15.478	15.406	9.900	...
1.77721	−1.39604	−1.09980	−0.403	0.109	0.025	0.046	5024.188	4990.005	0.022	0.005	0.024	0.036	17.375	16.719	9.900	...
1.90239	−1.31299	1.37664	0.387	−0.474	0.015	0.031	5022.109	5051.913	0.021	−0.021	0.019	0.029	17.443	16.765	9.900	...
...	...	...	...	...	...	...	...	...	...	...	...	...	...	...	...	...

→	$\sigma_{m_{\rm F814W}}$ (17)	${\tt QFIT}_{\rm F606W}$ (18)	${\tt QFIT}_{\rm F814W}$ (19)	$\chi^2_{\mu_\alpha \cos\delta}$ (20)	$\chi^2_{\mu_\delta}$ (21)	$\sigma_{\overline{x}}$ (22)	$\sigma_{\overline{y}}$ (23)	time (24)	${\rm err}_{\overline{x}}$ (25)	${\rm err}_{\overline{y}}$ (26)	$\rm U_{ref}$ (27)	$\rm N_{found}$ (28)	$\rm N_{used}$ (29)	ID (30)	$\Delta\mu_\alpha \cos\delta$ (31)	$\Delta\mu_\delta$ (32)
...	9.900	0.080	0.056	2.412	2.116	0.0018	0.0017	6.96206	0.0018	0.0016	1	30	24	86023	0.004	0.005
...	9.900	0.331	0.347	2.328	11.882	0.0134	0.0749	1.48741	0.0153	0.0350	0	26	15	86021	0.023	−0.079
...	9.900	0.084	0.049	3.502	2.750	0.0020	0.0022	6.96206	0.0019	0.0017	0	20	18	86020	0.047	0.013
...	9.900	0.062	0.043	1.706	4.652	0.0011	0.0019	6.96206	0.0011	0.0018	0	25	23	86022	0.049	0.014
...	9.900	0.118	0.063	1.279	0.796	0.0014	0.0011	6.96206	0.0013	0.0010	1	24	21	86019	0.017	−0.002
...	9.900	0.115	0.117	1.475	2.553	0.0016	0.0021	6.96206	0.0015	0.0020	1	25	23	86018	−0.006	0.017
...	9.900	0.080	0.084	1.045	2.306	0.0010	0.0017	6.96206	0.0010	0.0016	1	27	26	86483	0.022	−0.028
...	9.900	0.046	0.042	1.746	1.067	0.0015	0.0011	6.96195	0.0014	0.0011	0	16	14	86228	0.033	0.001
...	9.900	0.098	0.068	1.140	2.624	0.0013	0.0020	6.96206	0.0013	0.0021	1	25	25	86481	−0.010	0.011
...	9.900	0.146	0.096	0.895	2.024	0.0013	0.0016	6.96206	0.0012	0.0018	1	27	26	86485	−0.010	0.005
...	...	...	...	...	...	...	...	...	...	...	...	...	...	...	...	...

(This table is available in its entirety in a machine-readable form in the online journal. A portion is shown here for guidance regarding its form and content.)

REFERENCES

Anderson, J., & Bedin, L. R. 2010, PASP, 122, 1035
Anderson, J., Bedin, L. R., Piotto, G., Yadav, R. S., & Bellini, A. 2006, A&A, 454, 1029
Anderson, J., & King, I. R. 2003a, PASP, 115, 113
Anderson, J., & King, I. R. 2003b, AJ, 126, 772
Anderson, J., & King, I. R. 2006a, ACS/ISR 2006-01 (Baltimore, MD: STScI), available online at http://www.stsci.edu/hst/acs/documents/isrs
Anderson, J., & King, I. R. 2006b, ACS/ISR 2004-15 (Baltimore, MD: STScI), available online at http://www.stsci.edu/hst/acs/documents/isrs
Anderson, J., Sarajedini, A., Bedin, L. R., et al. 2008, AJ, 135, 2055
Anderson, J., & van der Marel, R. P. 2010, ApJ, 710, 1032
Beccari, G., Ferraro, F. R., Possenti, A., et al. 2006, AJ, 131, 2551
Bedin, L. R., Piotto, G., King, I. R., & Anderson, J. 2003, AJ, 126, 247
Bellini, A., Anderson, J., & Bedin, L. R. 2011, PASP, 123, 622
Bellini, A., & Bedin, L. R. 2009, PASP, 121, 1419
Bellini, A., Bedin, L. R., Pichardo, B., et al. 2010, A&A, 513, A51
Bellini, A., Piotto, G., Bedin, L. R., et al. 2009, A&A, 493, 959
Bellini, A., Piotto, G., Milone, A. P., et al. 2013, ApJ, 765, 32
Bianchini, P., Varri, A. L., Bertin, G., & Zocchi, A. 2013, ApJ, 772, 67
Binney, J., & Mamon, G. A. 1982, MNRAS, 200, 361
Cudworth, K. M. 1976, AJ, 81, 519
Da Costa, G. S., Freeman, K. C., Kalnajs, A. J., Rodgers, A. W., & Stapinski, T. E. 1977, AJ, 82, 810
den Brok, M., van de Ven, G., van den Bosch, R., & Watkins, L. 2014, MNRAS, 438, 487
Dinescu, D. I., Girard, T. M., van Altena, W. F., Mendez, R. A., & Lopez, C. E. 1997, AJ, 114, 1014
Drukier, G. A., Slavin, S. D., Cohn, H. N., et al. 1998, AJ, 115, 708
Eichhorn, H., & Jefferys, W. H. 1971, PMcCo, 16, 267
Gebhardt, K., Pryor, C., O'Connell, R. D., Williams, T. B., & Hesser, J. E. 2000, AJ, 119, 1268
Gerssen, J., van der Marel, R. P., Gebhardt, K., et al. 2002, AJ, 124, 3270
Gnedin, O. Y., Zhao, H., Pringle, J. E., et al. 2002, ApJL, 568, L23
Goldsbury, R., Richer, H. B., Anderson, J., et al. 2010, AJ, 140, 1830
Harris, W. E. 1996, AJ, 112, 1487 (2010 edition)
Illingworth, G. 1976, ApJ, 204, 73
Malavolta, L., Sneden, C., Piotto, G., et al. 2014, AJ, 147, 25
Massari, D., Bellini, A., Ferraro, F. R., et al. 2013, ApJ, 779, 81
Massari, D., Mucciarelli, A., Ferraro, F. R., et al. 2014, ApJ, 791, 101
McLaughlin, D. E., Anderson, J., Meylan, G., et al. 2006, ApJS, 166, 249
McNamara, B. J., Harrison, T. E., & Anderson, J. 2003, ApJ, 595, 187 (McN03)
McNamara, B. J., Harrison, T. E., & Baumgardt, H. 2004, ApJ, 602, 264
McNamara, B. J., Harrison, T. E., Baumgardt, H., & Khalaj, P. 2012, ApJ, 745, 175
McNamara, B. J., & McKeever, J. 2011, AJ, 142, 163
Milone, A. P., Piotto, G., Bedin, L. R., et al. 2012, A&A, 540, A16
Milone, A. P., Villanova, S., Bedin, L. R., et al. 2006, A&A, 456, 517
Peterson, R. C., & Cudworth, K. M. 1994, ApJ, 420, 612
Peterson, R. C., Seitzer, P., & Cudworth, K. M. 1989, ApJ, 347, 251
Piotto, G., Milone, A. P., Bedin, L. R., et al. 2014, arXiv:1410.4564
Rees, R. F., Jr. 1995, PhD thesis, Univ. Chicago, IL, USA
Rees, R. F., Jr. 1997, in ASP Conf. Ser. 127, Proper Motions and Galactic Astronomy, ed. R. M. Humphreys (San Francisco, CA: ASP), 109
Sabbi, E., & Bellini, A. 2013, WFC3/ISR 2013-11 (Baltimore, MD: StscI), available online at http://www.stsci.edu/hst/wfc3/documents/ISRs
Trenti, M., & van der Marel, R. 2013, MNRAS, 435, 3272
van der Marel, R. P., & Anderson, J. 2010, ApJ, 710, 1063
van der Marel, R. P., Anderson, J., Bellini, A., et al. 2014, in ASP Conf. Ser. 480, Structure and Dynamics of Disk Galaxies, ed. M. S. Seigar & P. Treuthardt (San Francisco, CA: ASP), 43
van Leeuwen, F., Le Poole, R. S., Reijns, R. A., Freeman, K. C., & de Zeeuw, P. T. 2000, A&A, 360, 472